J. Fluid Mech. (2002), *vol.* 468, *pp.* 205–237.
DOI: 10.1017/S0022112002001544 Printed in the United Kingdom

Dynamic simulations of the inhomogeneous sedimentation of rigid fibres

By JASON E. BUTLER† AND ERIC S. G. SHAQFEH

Department of Chemical Engineering, Stanford University, Stanford, CA 94305-5025, USA

(Received 17 April 2001 and in revised form 17 April 2002)

We have simulated the dynamics of suspensions of fibres sedimenting in the limit of zero Reynolds number. In these simulations, the dominant inter-particle force arises from hydrodynamic interactions between the rigid, non-Brownian fibres. The simulation algorithm uses slender-body theory to model the linear and rotational velocities of each fibre. To include far-field interactions between the fibres, the line distribution of force on each fibre is approximated by making a Legendre polynomial expansion of the disturbance velocity on the fibre, where only the first two terms of the expansion are retained in the calculation. Thus, the resulting linear force distribution can be specified completely by a centre-of-mass force, a couple, and a stresslet. Short-range interactions between particles are included using a lubrication approximation, and an infinite suspension is simulated by using periodic boundary conditions. Our numerical results confirm that the sedimentation of these non-spherical, orientable particles differs qualitatively from the sedimentation of spherical particles. The simulations demonstrate that an initially homogeneous, settling suspension develops clusters, or streamers, which are particle rich surrounded by clarified fluid. The instability which causes the heterogeneous structure arises solely from hydrodynamic interactions which couple the particle orientation and the sedimentation rate in particle clusters. Depending upon the concentration and aspect ratio, the formation of clusters of particles can enhance the sedimentation rate of the suspension to a value in excess of the maximum settling speed of an isolated particle. The suspension of fibres tends to orient with gravity during the sedimentation process. The average velocities and orientations, as well as their distributions, compare favourably with previous experimental measurements.

1. Introduction

The idea that the sedimentation of non-spherical, orientable particles differs qualitatively from the sedimentation of spherical particles is currently supported by theoretical calculations and experimental evidence. In the limit of sedimentation at zero Reynolds number and in the absence of Brownian motion (infinite Péclet number) as well as nonhydrodynamic interparticle forces, an initially homogeneous suspension of rigid fibres can develop clusters or streamers which are particle rich, surrounded by clarified fluid. Though the particles are non-colloidal, they appear to flocculate during sedimentation as observed in the experiments of Herzhaft *et al.* (1996) and Herzhaft & Guazzelli (1999). In contrast, sedimenting suspensions of

† Present address: Department of Chemical Engineering, The University of Florida, PO Box 116005, Gainesville, FL 32611-6005, USA.

spherical particles apparently do not suffer from a similar instability in particle concentration.

The instability of a suspension of fibres during sedimentation was originally predicted by the calculations of Koch & Shaqfeh (1989). The instability arises from the coupling of sedimentation velocity and particle orientation which renders the homogeneous settling state unstable to fluctuations in the particle volume fraction. Koch & Shaqfeh (1989) showed that hydrodynamic interactions between pairs of sedimenting spheroids induces a preferential alignment of the fibres which leads to a decrease in the average separation distance. A subsequent analysis of the stability of a suspension to horizontal fluctuations in the concentration of particles suggested that the particles would form streamers in the direction of gravity. In regions where the perturbed particle concentration is higher than in the bulk of the suspension, there is a downward convection of particles. In the less concentrated regions, the fluid primarily moves in the direction opposite to gravity. The relative shear between the high and low regions of concentration induces an alignment of fibres which causes a preference for particles to drift towards the concentrated region, thus magnifying the concentration gradient. Additionally, Koch & Shaqfeh (1989) suggested that the clustering of particles would result in an enhanced rate of sedimentation.

Given the importance of sedimentation to natural phenomena such as the deposit of river sediment and to industrial processes such as particulate separations, both experimental and numerical work has been pursued by researchers in order to ascertain the accuracy and implications of the calculations made by Koch & Shaqfeh (1989). Experiments by Herzhaft *et al.* (1996) and Herzhaft & Guazzelli (1999) have confirmed the existence of an instability. In these experiments, suspensions of glass rods sedimenting within a fluid with a refractive index which matched that of the particles were examined. A small fraction of the particles were marked and then tracked with a digital imaging system during the sedimentation process. Particle velocities, fluctuations, and orientations of the fibres were studied for a range of particle aspect ratios and number densities within the dilute and semi-dilute concentration regimes.

As already mentioned, these experiments gave visual verification of the instability of fibre sedimentation; pictures of the sedimenting suspension clearly show the presence of large-scale inhomogeneities in the particle distribution. The experiments also show that particles tend to align in the gravitational direction. For small number densities, the sedimentation velocity was found to exceed the rate expected for a well-mixed, homogeneous suspension. For some fibre aspect ratios and concentrations, the suspension was found to sediment with a velocity in excess of the settling velocity of an isolated fibre which is aligned with gravity and sedimenting in a fluid of infinite extent.

Other experiments on the sedimentation of non-Brownian fibres include those of Turney *et al.* (1995). Using magnetic resonance imaging, they estimated the settling velocity from measurements of the time variation of the diffuse interface between the supernatant and suspension. No evidence of an instability was observed since these measurements were made for volume fractions higher than the volume fractions at which other workers have observed enhanced sedimentation velocities. The sedimentation rates were found to agree well with those measured by Herzhaft & Guazzelli (1999) at the same concentrations.

In addition to these experimental studies, simulations of sedimentation for suspensions of rigid fibres of high aspect ratio have also been completed. Claeys & Brady (1993*c*) simulated the sedimentation of a periodic array of spheroids using the algorithm described in Claeys & Brady (1993*a*, *b*). The method is similar to the

Stokesian dynamics method which has been successfully used to simulate suspensions of spherical particles (Durlofsky, Brady & Bossis 1987; Brady & Bossis 1988). Claeys & Brady (1993*c*) calculated the sedimentation rate as a function of concentration, but the particles were confined to an organized, crystalline lattice for these simulations. Thus, the results were unable to predict the change in orientation distribution, centre-of-mass distribution, sedimentation velocity, and other properties which occurs in a disordered suspension.

In a recent work, Kuusela, Höfler & Schwarzer (2001) calculated the dynamics of a suspension of spheroids of aspect ratio 5 sedimenting at a finite Reynolds number of 0.3. The calculation was made using a finite difference method as described in detail by Höfler & Schwarzer (2000). The calculations of Höfler & Schwarzer (2000) showed that a fibre which falls at a small, but finite, Reynolds number will rotate until the orientation becomes horizontal. This is an important difference compared to sedimentation of fibres in the Stokes regime, or in the limit of zero Reynolds number; in that case an isolated fibre will not change orientation during sedimentation. Observations made in the experiments of Herzhaft *et al.* (1996) and Herzhaft & Guazzelli (1999) indicate that an individual fibre falls without changing orientation. Thus the orientation of fibres in the experiments is influenced only by hydrodynamic interactions with other fibres and the walls, and not influenced by inertia. Even though the fibres in the simulations of Kuusela *et al.* (2001) are influenced by the affects of inertia, the results do show some similar behaviour to the experiments. For example, the results indicate that as the volume fraction of the particles increases, the average sedimentation velocity begins to increase and then decreases. However, the maximum in the average sedimentation rate of the particles did not exceed the sedimentation velocity of a particle aligned with gravity as observed in the experiments. This maximum was mainly attributed to the change in the average orientation of the particles at steady state as a function of the bulk value of the particle number density. The authors state that a 'visual inspection' of the structure of the simulated suspension reveals a non-homogeneous distribution of spheroids, but unfortunately, no attempt was made to quantify the centre-of-mass distribution of the particles.

Mackaplow & Shaqfeh (1998) reported on the results from two types of simulations: Monte Carlo simulations and point-particle simulations. They performed Monte Carlo simulations to calculate the average velocities of sedimentation assuming a statistical distribution of particle positions and orientations. Evolving the particle positions in time when using their method was, however, too computationally intensive. To overcome this difficulty, dynamic point-particle simulations were developed by Mackaplow & Shaqfeh (1998). In this method, the disturbance due to a point force replaces the disturbance due to a fibre and the mobility of each point force depends on the orientation in the same manner as that of a rigid fibre of high aspect ratio. Using these simplifications, which are appropriate in the dilute regime, dynamic simulations were completed. The simulations showed that fibres in a suspension with initially homogeneous distributions of the centre of mass and orientation develop an orientation which is preferentially aligned with the gravitational direction. The particles also cluster and the sedimentation velocity increases as a result. However, the simulation was unable to predict a steady sedimentation rate for the particles.

In the present study, we have developed a simulation algorithm which accounts for the finite length of the particles when calculating the interparticle hydrodynamic interactions. The algorithm is sufficiently efficient to enable dynamic simulations and we are able to determine a convergent, steady-state sedimentation velocity for a given set of parameter values. The results capture the essence of published experimental

observations, and for many of the details, the calculations agree quantitatively with the data of Herzhaft & Guazzelli (1999).

In § 2, the numerical method for simulating the sedimentation of a suspension of fibres is presented in detail. The results of the simulations follow in § 3 along with a detailed comparison to existing experiments. In § 4 we present an overview of the success of our simulations and we summarize and conclude in § 5.

2. Simulation method

To calculate the 'far-field' inter-particle hydrodynamic interactions, our simulation method uses slender-body theory together with a linearization of the force distribution along the centreline of each fibre. The linearized specification of the force density includes a force on the centre of mass, a couple, and a stresslet on each fibre as demonstrated below. Note that we do not assume point-singularity interactions, but rather a linear force distribution along the fibres. The method is similar to that used by Harlen, Sundararajakumar & Koch (1999) who simulated a sphere falling through a neutrally buoyant suspension of rigid rods. Our particular simulation method differs in that the suspension is made entirely of fibres which are not neutrally buoyant and periodic boundary conditions are used to simulate an infinite suspension. Also, the short-range hydrodynamic forces are calculated using a lubrication approximation instead of irreversible contacts between particles as was employed by Harlen *et al.* (1999). The details of the calculations for the far-field interaction are presented in § 2.1. A discussion of the method used to include lubrication is in § 2.3 and then the complete set of equations is given in § 2.4.

2.1. *Far-field interactions*

For our simulation method the linear and rotational velocities of each fibre are described by the slender-body theory of Batchelor (1970). For a leading-order approximation in $\log(2A)$, where A is the aspect ratio, the equation relates the motion of the fibre to the force distribution by the fibre acting on the fluid,

$$\dot{\boldsymbol{x}}_\alpha + s\dot{\boldsymbol{p}}_\alpha - \boldsymbol{u}'_\alpha = \frac{\log(2A)}{4\pi}(\boldsymbol{I} + \boldsymbol{p}_\alpha\boldsymbol{p}_\alpha)\cdot\boldsymbol{f}_\alpha(s), \tag{2.1}$$

where $\boldsymbol{x}_\alpha$ and $\dot{\boldsymbol{x}}_\alpha$ are the vectors specifying the position and velocity of the centre of mass of fibre α. The unit vector $\boldsymbol{p}_\alpha$ describes the orientation of the fibre α and $\dot{\boldsymbol{p}}_\alpha$ is the rotational velocity. The disturbance velocity, $\boldsymbol{u}'_\alpha$, is the sum of the imposed velocity field and the fluid velocities caused by the particles other than α. The motion of the slender body also depends upon the aspect ratio A (total length to diameter) and the distribution of forces $\boldsymbol{f}_\alpha(s)$ along the length s of the fibre.

In the simulation method of Claeys & Brady (1993*a*), the development of the algorithm begins with the singularity solution of Chwang & Wu (1974, 1975) for the motion of spheroids instead of the slender-body equation as here. Since the formulations are consistent in the limit of high aspect ratio (Kim & Karrila 1991), no important details are lost in the calculation so long as the simulations are limited to rigid fibres of high aspect ratio.

Integrating equation (2.1) over the length of the fibre gives an explicit relationship for translational velocity as functions of the force and velocity along the fibre,

$$\dot{\boldsymbol{x}}_\alpha = \frac{1}{2}\int_{-1}^{1}\boldsymbol{u}'_\alpha(\boldsymbol{x}_\alpha + s\boldsymbol{p}_\alpha)\,\mathrm{d}s + \frac{\log(2A)}{8\pi}(\boldsymbol{I} + \boldsymbol{p}_\alpha\boldsymbol{p}_\alpha)\cdot\boldsymbol{F}_\alpha. \tag{2.2}$$

Likewise, taking the cross-product of equation (2.1) with $s\boldsymbol{p}_\alpha$ and then integrating over the length of the fibre gives the corresponding expression for the rotational velocity for fibre α,

$$\dot{\boldsymbol{p}}_\alpha = \tfrac{3}{2}(\boldsymbol{I} - \boldsymbol{p}_\alpha\boldsymbol{p}_\alpha)\cdot\int_{-1}^{1} s\boldsymbol{u}'_\alpha \,\mathrm{d}s - \frac{3\log(2A)}{8\pi}\boldsymbol{p}_\alpha \wedge \mathscr{T}_\alpha. \tag{2.3}$$

In the preceding equations, the integrated force and torque are

$$\boldsymbol{F}_\alpha = \int_{-1}^{1} \boldsymbol{f}_\alpha(s)\,\mathrm{d}s, \tag{2.4}$$

$$\mathscr{T}_\alpha = \int_{-1}^{1} s\boldsymbol{p}_\alpha \wedge \boldsymbol{f}_\alpha(s)\,\mathrm{d}s, \tag{2.5}$$

and the equations have been made dimensionless with a characteristic length, time and velocity given by

$$\left.\begin{aligned} u_c &= \frac{gV\Delta\rho}{4\pi\mu l}\log(2A), \\ l_c &= l, \\ t_c &= l_c/u_c = \frac{4\pi\mu l^2}{gV\Delta\rho\log(2A)}. \end{aligned}\right\} \tag{2.6}$$

The volume and reduced density of a fibre is respectively V and $\Delta\rho$. The fluid viscosity is denoted by μ and gravitational acceleration by g. The half-length of a fibre is l. Thus, the characteristic velocity equals the velocity of an isolated fibre falling with an orientation parallel to gravity, while the characteristic time is the time needed for such a fibre to sediment half of its length.

In the original analysis of Batchelor (1970), the slender-body approximation was derived from a boundary integral equation where, under the assumption that the error is small since the aspect ratio is high, the surface integral is computed as a line integral along the centreline of the particle. Thus, the velocity disturbance generated by particle β at a position $\boldsymbol{x}$ can be approximated as

$$\boldsymbol{u}_\beta(\boldsymbol{x}) = \int_{-1}^{1} \boldsymbol{J}(\boldsymbol{x} - \boldsymbol{x}_\beta - s\boldsymbol{p}_\beta)\cdot\boldsymbol{f}_\beta(s)\,\mathrm{d}s, \tag{2.7}$$

where $\boldsymbol{J}$ is the Oseen tensor,

$$\boldsymbol{J}(\boldsymbol{x} - \boldsymbol{\xi}) = \frac{1}{8\pi}\left(\frac{\boldsymbol{I}}{R} + \frac{(\boldsymbol{x} - \boldsymbol{\xi})(\boldsymbol{x} - \boldsymbol{\xi})}{R^3}\right), \tag{2.8}$$

and R is the distance between the evaluation point and a point force located at position $\boldsymbol{\xi}$.

Equation (2.7) represents the disturbance velocity created by a single fibre, but to simulate an infinite suspension the disturbance velocity for an array of fibres is needed. Since we will approximate an infinite suspension by imposing periodic boundary conditions on a simulation box, the Oseen tensor must be replaced by the fundamental solution $\boldsymbol{J}_p$ of the Stokes equations for a periodic array of point forces as derived by Hasimoto (1959). Since an imposed or mean flow does not exist for this particular problem, the disturbance velocity on a given fibre arises solely from

the motion of the other fibres,

$$\boldsymbol{u}'_\alpha(\boldsymbol{x}_\alpha + s_\alpha \boldsymbol{p}_\alpha) = \sum_{\beta=1}^{N} \int_{-1}^{1} \boldsymbol{K}(\boldsymbol{x}_\alpha + s_\alpha \boldsymbol{p}_\alpha - \boldsymbol{x}_\beta - s_\beta \boldsymbol{p}_\beta) \cdot \boldsymbol{f}_\beta(s_\beta)\, \mathrm{d}s_\beta, \tag{2.9}$$

where

$$\boldsymbol{K}(\boldsymbol{x}_\alpha + s_\alpha \boldsymbol{p}_\alpha - \boldsymbol{x}_\beta - s_\beta \boldsymbol{p}_\beta) = \begin{cases} \boldsymbol{J}_p(\boldsymbol{x}_\alpha + s_\alpha \boldsymbol{p}_\alpha - \boldsymbol{x}_\beta - s_\beta \boldsymbol{p}_\beta) & \text{if} \quad \alpha \neq \beta, \\ \boldsymbol{J}_p(s_\alpha - s_\beta) - \boldsymbol{J}(s_\alpha - s_\beta) & \text{if} \quad \alpha = \beta. \end{cases} \tag{2.10}$$

The Oseen tensor must be subtracted from the periodic fundamental solution for the second case in equation (2.10) when $\alpha = \beta$ so that the velocity due to fibre α is not included in the calculation of the disturbance velocity. In the event that $\alpha = \beta$ and $s_\alpha = s_\beta$, the limiting form of the matrix $\boldsymbol{J}_p - \boldsymbol{J}$ which was derived by Hasimoto (1959) must be used. Evaluating the periodic fundamental solution is a time-consuming calculation which involves an infinite sum. However, the burden is substantially reduced by using Ewald sums (Hasimoto 1959).

In a manner similar to that of Mackaplow & Shaqfeh (1998), at this point we could discretize each fibre and solve the set of equations directly for the force distribution and velocity disturbance on each fibre. Such a solution method is computationally expensive, however, and severely limits the time span over which the sedimenting suspension can be simulated. Mackaplow & Shaqfeh (1998) carried out Monte Carlo simulations with preassigned, uniform distributions of particles and did not solve for the dynamic evolution of the suspension microstructure. A more efficient approach is needed to overcome the computational expense while still including the effect of multi-body interactions and preserving the effect of finite particle length, thus avoiding the point-particle approximation of Mackaplow & Shaqfeh (1998).

2.2. *Linearization of force distribution*

Linearizing the force distribution for the fibres as was accomplished by Harlen *et al.* (1999) makes the problem of solving for the dynamic evolution of the particle structure feasible. Using equations (2.1), (2.2) and (2.3) to solve for the force distribution in terms of the velocity disturbance and the total force and torque on the particle gives

$$\begin{aligned} \boldsymbol{f}_\alpha = \frac{2\pi}{\log(2A)} \left(\boldsymbol{I} - \tfrac{1}{2}\boldsymbol{p}_\alpha \boldsymbol{p}_\alpha\right) \cdot \int_{-1}^{1} \boldsymbol{u}'_\alpha \,\mathrm{d}s + \tfrac{1}{2}\boldsymbol{F}_\alpha + \frac{3s}{2} \left[\frac{4\pi}{\log(2A)} (\boldsymbol{I} - \boldsymbol{p}_\alpha \boldsymbol{p}_\alpha) \right. \\ \left. \times \int_{-1}^{1} s\boldsymbol{u}'_\alpha \,\mathrm{d}s + \mathscr{T}_\alpha \wedge \boldsymbol{p}_\alpha \right] - \frac{4\pi}{\log(2A)} \left(\boldsymbol{I} - \tfrac{1}{2}\boldsymbol{p}_\alpha \boldsymbol{p}_\alpha\right) \cdot \boldsymbol{u}'_\alpha. \end{aligned} \tag{2.11}$$

Expanding the disturbance velocity in a series of Legendre polynomials in the fibre coordinate s and retaining only the first two terms results in a spectral approximation $\tilde{\boldsymbol{u}}'_\alpha(s)$ of the disturbance velocity $\boldsymbol{u}'_\alpha(s)$,

$$\tilde{\boldsymbol{u}}'_\alpha(s) = \frac{1}{2} \int_{-1}^{1} \boldsymbol{u}'_\alpha \,\mathrm{d}s + \frac{3s}{2} \int_{-1}^{1} s\boldsymbol{u}'_\alpha \,\mathrm{d}s, \tag{2.12}$$

where $\boldsymbol{u}'_\alpha(s)$ is evaluated using equation (2.9). Using the approximation $\tilde{\boldsymbol{u}}'_\alpha(s)$ in place of $\boldsymbol{u}'_\alpha(s)$ in equation (2.11) gives a linear form for the force distribution,

$$\boldsymbol{f}_\alpha(s) = \tfrac{1}{2}\boldsymbol{F}_\alpha + \tfrac{3}{2}s(\mathscr{T}_\alpha \wedge \boldsymbol{p}_\alpha + \mathscr{S}_\alpha \boldsymbol{p}_\alpha), \tag{2.13}$$

which is the linear force distribution used by Harlen *et al.* (1999).

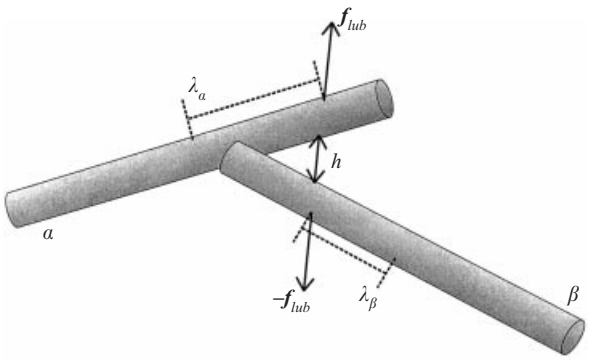

FIGURE 1. The lubrication force $\boldsymbol{f}_{lub}$ between two fibres α and β. As shown, the force acts on fibre α at $s = \lambda_\alpha$ and acts on fibre β at $s = \lambda_\beta$ in the opposite direction.

The net hydrodynamic force, $\boldsymbol{F}_\alpha$, must balance the sum of the force due to gravity, $\boldsymbol{F}_g$, as well as the forces due to lubrication, which are discussed in § 2.3. There is no torque on a particle due to gravity, so the net hydrodynamic torque, $\mathscr{T}_\alpha$, is equal to the sum of the torques created on fibre α by the lubrication interactions. The third term in equation (2.13) includes the stresslet $\mathscr{S}_\alpha$ for fibre α, where

$$\mathscr{S}_\alpha = -\frac{2\pi}{\log(2A)} \int_{-1}^{1} s\boldsymbol{p}_\alpha \cdot \boldsymbol{u}'_\alpha \, \mathrm{d}s. \tag{2.14}$$

Since the particles possess only one finite dimension, the stresslet is a scalar quantity which arises from the inability of a fibre to stretch or compress along its major axis.

The stresslet in equations (2.13) and (2.14) incorporates multi-body hydrodynamic interactions into the simulation method. Equation (2.14) is used to solve directly for the value of the stresslet $\mathscr{S}_\alpha$ for every fibre α. The disturbance velocity in the equation for the stresslet is evaluated using equation (2.9) with the force distribution given by equation (2.13). The final result is a linear set of equations for the stresslets which depends upon the instantaneous configuration of all the particles within the suspension. In turn, the stresslets are used in equations (2.2) and (2.3) to calculate the motion of the fibres. This is demonstrated in § 2.4, but first the method for including lubrication interactions is presented.

2.3. *Lubrication interactions*

When the minimum separation between two particles approaches and falls below one fibre diameter, lubrication dominates the interactions of the pair. These short-range interactions between particles are included using lubrication approximations derived from the formulas of Claeys & Brady (1989).

For the case of fibres α and β interacting along their length as seen in figure 1, the approximate force acting on fibre α is

$$\boldsymbol{f}_{lub} = -\frac{6\pi\dot{h}}{A^2 \, |\boldsymbol{p}_\alpha \wedge \boldsymbol{p}_\beta| \, h}\boldsymbol{n}, \tag{2.15}$$

where $\boldsymbol{n}$ is the unit vector normal to the orientation of both fibres and is given by

$$\boldsymbol{n} = \pm\frac{\boldsymbol{p}_\alpha \wedge \boldsymbol{p}_\beta}{|\boldsymbol{p}_\alpha \wedge \boldsymbol{p}_\beta|}. \tag{2.16}$$

The normal points from fibre α to fibre β, so the sign is chosen accordingly. The force on fibre β is equivalent, but acts in the opposite direction. The minimum separation distance is

$$h = |(\boldsymbol{x}_\alpha - \boldsymbol{x}_\beta) \cdot \boldsymbol{n}| - \frac{1}{A} \tag{2.17}$$

and $\dot{h}$ is the relative velocity between the two fibres projected along their common normal,

$$\dot{h} = \left(\dot{\boldsymbol{x}}_\alpha + \lambda_\alpha \dot{\boldsymbol{p}}_\alpha - \dot{\boldsymbol{x}}_\beta - \lambda_\beta \dot{\boldsymbol{p}}_\beta\right) \cdot \boldsymbol{n}. \tag{2.18}$$

In this equation, λ_α and λ_β are the points on the respective fibres where the distance between the fibres is minimum and where the lubrication force acts.

The preceding analysis is similar to that suggested by Yamane, Kaneda & Doi (1994) and which has been used in simulations of shear flow of rigid fibres by Fan, Phan-Thien & Zheng (1998). In their simulations, as well as in this algorithm, the tangential components of the lubrication interactions are not included. The lubrication force due to relative, tangential motion of the fibres scales as $\log(1/h)$, and thus is much smaller than the normal component of the lubrication force.

Equation (2.15) is an approximation of the lubrication force between two non-parallel cylindrical bodies of infinite length. However, if the fibres are nearly parallel, the relationship fails since the parallel limit is singular for infinitely long fibres. Of course, in fact the fibres have a finite length, even if large with respect to the diameter. To account for the finite length in the event of a short-range interaction between parallel particles, the lubrication equations of Claeys & Brady (1989) are implemented using a dimensional radius of curvature equal to the particle length. The resulting lubrication force is given by

$$\boldsymbol{f}_{lub} = -\frac{12\pi\dot{h}}{(2A+1)\left[\left(A^2+1/4\right)|\boldsymbol{p}_\alpha \wedge \boldsymbol{p}_\beta|^2 + A\left(1+\left(\boldsymbol{p}_\alpha \cdot \boldsymbol{p}_\beta\right)^2\right)\right]^{1/2} h}\boldsymbol{n}. \tag{2.19}$$

The preceding equation is well defined for parallel rods and reduces to the previous expression of equation (2.15) for a large aspect ratio and alignment which is not parallel. When two fibres are parallel or nearly parallel ($|\boldsymbol{p}_\alpha \cdot \boldsymbol{p}_\beta| \leqslant 0.999$), equation (2.19) is used within the numerical algorithm to calculate the lubrication force instead of equation (2.15).

For the far-field hydrodynamic interactions, the details of the end interactions between fibres have no effect. However, when calculating the lubrication interactions, those details must be included. These additional types of interactions are handled in the same manner as above using the lubrication analysis of Claeys & Brady (1989) with the ends of the particles modelled as spherical caps. For an end-cap interacting with a cylindrical body, the lubrication force is given by

$$\boldsymbol{f}_{lub} = -\frac{4\pi\dot{h}}{\sqrt{2}A^2 h}\boldsymbol{n}. \tag{2.20}$$

For an end-cap interacting with another end-cap, the lubrication is approximated by the formula for a sphere interacting with another sphere,

$$\boldsymbol{f}_{lub} = -\frac{3\pi\dot{h}}{2A^2 h}\boldsymbol{n}. \tag{2.21}$$

In the previous two equations, the normal vector is given by a relationship different from that described by equation (2.16) and the minimum separation distance h must also be calculated using the appropriate relationship.

In the simulation algorithm, lubrication interactions are assumed negligible for pairs of fibres with a minimum separation distance greater than one fibre diameter. To calculate the lubrication forces, the number and type of interactions must first be identified. For every fibre pair meeting the requirement $h \leqslant 2/A$, the lubrication force must be determined using the lubrication equation corresponding to the relative geometries of the two fibres. Since the lubrication forces and stresslet given by equation (2.14) depend on one another, the solution must be made simultaneously. Thus, the solution requires solving a set of linear equations with an equation for each stresslet and an additional equation for each lubrication force.

As is commonly practised with Stokesian dynamics (Durlofsky & Brady 1989), each lubrication interaction is supplemented with a small, repulsive force which acts at the same points and in the same direction as the lubrication force. The purpose of including this force is to keep the minimum separation distance between the particles from becoming, or remaining, artificially small due to small errors in the integration with respect to time. The form of the repulsive force is

$$\boldsymbol{f}_r = a_o \frac{\tau \mathrm{e}^{-\tau h}}{1 - \mathrm{e}^{-\tau h}} \boldsymbol{n}, \tag{2.22}$$

which is the same expression as used by Durlofsky & Brady (1989). The parameters a_o and τ are selected so that the force is small over most of the range of the lubrication force. For most of the simulations, the dimensionless values of a_o and τ were respectively set equal to 1×10^{-4} and 1×10^{3}. The dimensional form of a_o is given by multiplying by $\mu l_c^2 u_c$ and the dimensional value for τ is given by dividing by the characteristic length, l. The values of both a_o and τ were also varied to confirm that they had little impact upon the simulation results.

In their simulation of a sphere falling through a viscous suspension of rigid rods, Harlen *et al.* (1999) ignored lubrication and the excluded volume of the rods and allowed the centrelines of the fibres to contact, but not pass through, each other. Unfortunately, rigorous solution of the contact forces for particles with multiple contacts is a nonlinear problem. Harlen *et al.* (1999) overcame this problem by implementing some simplifying rules to define the particle contacts. In the present case, however, large rafts of interconnected, contacting fibres form and the rules suggested by Harlen *et al.* (1999) to define contacts fail.

Not allowing contact interactions saves computational time because the expensive search for collisions and the resulting iteration process for the particle velocities is avoided. However, small time steps become necessary to avoid the possibility of violating the excluded volume of the particles. As the aspect ratio increases, the problem of resolving lubrication interactions becomes more time consuming, scaling roughly with the aspect ratio.

2.4. *Complete equations*

Once the stresslets are computed along with any lubrication forces, the motion of each fibre can be determined by using equations (2.2) and (2.3). The disturbance velocity is evaluated using equation (2.9) and the force distribution is given by (2.13). Combining all of these equations results in the following two equations for the linear

and rotational velocities of the fibres:

$$\dot{\boldsymbol{x}}_\alpha = \sum_{\beta=1}^{N} \left(\mathscr{K}_{\alpha\beta} + \mathscr{S}_\beta \mathscr{P}_{\alpha\beta}\right) + \sum_{l=1}^{M} \mathscr{M}_{\alpha l} \cdot \boldsymbol{g}_l + \frac{\ln(2A)}{8\pi}(\boldsymbol{I} + \boldsymbol{p}_\alpha \boldsymbol{p}_\alpha) \cdot \left(\boldsymbol{F}_g + \sum_{k=1}^{M} \mathscr{A}_{\alpha k} \boldsymbol{g}_k\right), \tag{2.23}$$

$$\dot{\boldsymbol{p}}_\alpha = \sum_{\beta=1}^{N} \left(\mathscr{L}_{\alpha\beta} + \mathscr{S}_\beta \mathscr{Q}_{\alpha\beta}\right) + \sum_{l=1}^{M} \mathscr{N}_{\alpha l} \cdot \boldsymbol{g}_l + \frac{3\ln(2A)}{8\pi}(\boldsymbol{I} - \boldsymbol{p}_\alpha \boldsymbol{p}_\alpha) \cdot \sum_{k=1}^{M} \mathscr{B}_{\alpha k} \boldsymbol{g}_k. \tag{2.24}$$

The gravitational force, $\boldsymbol{F}_g$, has a direct effect on the sedimentation of a fibre as seen in equation (2.23), but does not have a direct effect on the rotational velocity. However, the sedimentation of each fibre causes a disturbance which can induce a rotation as well as a displacement of another fibre. The linear velocity of fibre α due to the gravitational force on fibre β is given by

$$\mathscr{K}_{\alpha\beta} = \frac{1}{4} \iint_{-1}^{1} \boldsymbol{K} \cdot \boldsymbol{F}_g \, \mathrm{d}s_\beta \, \mathrm{d}s_\alpha, \tag{2.25}$$

and the rotational velocity of α due to gravity acting on fibre β is given by

$$\mathscr{L}_{\alpha\beta} = \tfrac{3}{4}(\boldsymbol{I} - \boldsymbol{p}_\alpha \boldsymbol{p}_\alpha) \cdot \iint_{-1}^{1} \boldsymbol{K} \cdot \boldsymbol{F}_g \, \mathrm{d}s_\beta s_\alpha \, \mathrm{d}s_\alpha. \tag{2.26}$$

In these equations, the matrix $\boldsymbol{K}$ (defined in equation (2.10)) is a function of the relative spatial arrangement of the fibres α and β as well as the positions s_α and s_β on the length of the fibres.

The gravitational and lubrication forces acting on each fibre also influence the motion of the other fibres in the suspension through the stresslet. The sub-matrix $\mathscr{P}$ relates the stresslet on fibre β to the linear motion of fibre α, where each component takes the form

$$\mathscr{P}_{\alpha\beta} = \frac{3}{4} \iint_{-1}^{1} \boldsymbol{K} \cdot \boldsymbol{p}_\beta s_\beta \, \mathrm{d}s_\beta \, \mathrm{d}s_\alpha. \tag{2.27}$$

Likewise, the stresslet can cause a rotation as described by the relationship

$$\mathscr{Q}_{\alpha\beta} = \tfrac{9}{4}(\boldsymbol{I} - \boldsymbol{p}_\alpha \boldsymbol{p}_\alpha) \cdot \iint_{-1}^{1} \boldsymbol{K} \cdot \boldsymbol{p}_\beta s_\beta \, \mathrm{d}s_\beta s_\alpha \, \mathrm{d}s_\alpha. \tag{2.28}$$

The remaining terms in equations (2.23) and (2.24) arise from the lubrication forces which are denoted as $\boldsymbol{g}_i$, where the subscript identifies the particular interaction. The total number of interactions, M, depends upon the relative arrangement of the particles. Each interaction i is associated with a pair of particles which are labelled a and b; the force $\boldsymbol{g}_i$ is defined as positive on particle a and negative on b. The position on the fibre length at which interaction i acts upon fibre a is denoted λ_{ia}. To calculate the direct contribution to the velocities, the lubrication interactions are multiplied by the matrices

$$\mathscr{A}_{\alpha k} = \delta_{\alpha a} - \delta_{\alpha b}, \tag{2.29}$$

$$\mathscr{B}_{\alpha k} = \delta_{\alpha a}\lambda_{ka} - \delta_{\alpha b}\lambda_{kb}, \tag{2.30}$$

where $\delta_{\alpha a}$ equals zero unless $\alpha = a$, in which case it equals one. The indirect effect of

a lubrication force on fibre α appears in equations (2.23) and (2.24) as

$$\mathscr{M}_{\alpha l} = \frac{1}{4}\int\!\!\int_{-1}^{1} \boldsymbol{K}\cdot(\boldsymbol{I} + 3\lambda_{ka}s_a(\boldsymbol{I} - \boldsymbol{p}_a\boldsymbol{p}_a))\,\mathrm{d}s_a\,\mathrm{d}s_\alpha - \frac{1}{4}\int\!\!\int_{-1}^{1} \boldsymbol{K}\cdot(\boldsymbol{I} + 3\lambda_{kb}s_b(\boldsymbol{I} - \boldsymbol{p}_b\boldsymbol{p}_b))\,\mathrm{d}s_b\,\mathrm{d}s_\alpha, \quad (2.31)$$

$$\mathscr{N}_{\alpha l} = \tfrac{3}{4}(\boldsymbol{I} - \boldsymbol{p}_\alpha\boldsymbol{p}_\alpha)\cdot\left(\int\!\!\int_{-1}^{1} \boldsymbol{K}\cdot(\boldsymbol{I} + 3\lambda_{ka}s_a(\boldsymbol{I} - \boldsymbol{p}_a\boldsymbol{p}_a))\,\mathrm{d}s_a s_\alpha\,\mathrm{d}s_\alpha - \int\!\!\int_{-1}^{1} \boldsymbol{K}\cdot(\boldsymbol{I} + 3\lambda_{kb}s_b(\boldsymbol{I} - \boldsymbol{p}_b\boldsymbol{p}_b))\,\mathrm{d}s_b s_\alpha\,\mathrm{d}s_\alpha\right). \quad (2.32)$$

To numerically compute the integrals in the above equations, Gaussian quadrature is used to integrate over each length. For fibres separated by less than one fibre length, ten quadrature points were used for each integral, otherwise five points was sufficient to calculate the convergent values of the integrals.

After calculating the linear and rotational velocities using the relationships given in equation (2.23) and equation (2.24), a fourth-order Runge–Kutta method advances the particle positions and orientations in time. The time step is determined using an adaptive method. All pairs of particles which have a separation distance small enough to be affected by lubrication are analysed to determine if the separation distance is increasing or decreasing. For those pairs that are approaching each other, an estimate of the time to contact is calculated based upon the instantaneous geometry and relative velocity. The time step is then set equal to either 1/2 or 3/4 of the smallest estimated time to contact. In the rare event that there are no pairs of particles which are within lubrication range and which are approaching one another, the time step is selected so that no particle moves more than 1/2 of the diameter of the fibres.

Despite the precautions built into the adaptive method used to determine the time step, a collision or overlap of a pair of fibres does occasionally occur. In that event, the position and orientation of the rods are returned to the configuration which existed before the current time step began. The move is then tried again using a smaller time step equal to either 1/2 or 3/4 of the time step which was last attempted and failed.

The strict adherence to maintenance of the excluded volume of the fibres generally requires very small time steps since at least one pair of particles is often close to contact. After advancing the configuration of the fibres over the short time step, the lubrication forces may change significantly, but the long-range interactions essentially remain unaltered since the microstructure of the suspension changes very little. Therefore, the simulation method updates the lubrication interactions for each new position, but the long-range hydrodynamic interactions are updated less frequently. This use of this approximation greatly improves the run-time performance of the program with little or no impact upon the computational results.

Lubrication interactions were not included in some of the simulations in order to quantify the effect of short-range interactions. To advance the positions and orientations for these simulations, the Euler method was used instead of the Runge–Kutta algorithm and the necessity of maintaining the excluded volume was ignored. When using the Euler method, the dimensionless time step was chosen so that the particle possessing the maximum velocity would move no further than one tenth of its total length. Halving the time step in an example calculation demonstrated that

this criterion was sufficiently rigorous to give a convergent result for the average sedimentation velocity of the suspension of fibres as a function of time. Also, for these simulations, the hydrodynamic interactions were fully calculated at every step. We present results from calculations with and without lubrication interactions, as well as other results, in the next section.

3. Results

Using the numerical method described in the previous section, simulations were made for a range of parameters. Many of the simulation results are compared to experimental measurements. We first present results on the particle structure in § 3.1. The convergence of the average sedimentation velocity with particle number N is investigated next in § 3.2, and then the effect of the relative dimensions of the periodic simulation cell is studied in § 3.3. Information on the probability distribution of the fibre orientations as well as the dynamics of the particle orientations appears in § 3.4. Plots of the velocity distribution follow in § 3.5. Finally, in § 3.6 the effect of increasing the bulk number density on the average sedimentation velocity, velocity fluctuations, and orientation parameter are given for fibre aspect ratios of 11 and 32.

3.1. *Particle distribution*

Direct visualization of the suspension demonstrates that the simulation predicts the formation of clusters of particles. Snapshots of the suspension structure appear in figure 2 for a bulk number density of 0.154, an aspect ratio $A = 11$, and a height to width ratio of $d_z/d_w = 2$ for the periodic cell. For this simulation, and all of the simulations presented in this paper, the periodic cell has a square cross-section in the horizontal plane where d_w is the dimensionless width of the cell in the x- and y-directions as designated by d_x and d_y. The length of the periodic cell in the gravitational direction, d_z, is not generally equal to d_w. The number of particles per cell for the simulation shown in figure 2 equals 128 and lubrication was not included in this particular calculation.

Initially, at $t = 0$, the particles in the suspension are uniformly distributed in space and in orientation. By $t = 40$, the particles have preferentially aligned in the gravitational direction and a noticeable lack of uniformity in the spatial distribution already exists. The same trend is evident in the data for $t = 80$, and at $t = 120$ the inhomogeneity in particle distribution has become even more apparent. The clustering of particles is most pronounced in the directions perpendicular to gravity and the cluster is elongated in the direction of gravity.

Though the region of high particle concentration, or cluster, moves through the periodic cell continuously and smoothly during the simulation, the cluster is not composed of a fixed subset of the particles in the suspension. Rather, once the average structure has attained a steady configuration at $t = 120$, individual particles continue to enter and exit the cluster.

For the data shown in figure 2 at $t = 120$, a vertical average of the particle centre of mass as a function of horizontal position was made. The result, shown in figure 3(a), demonstrates that the particle concentration at the peak value is roughly ten times that of the bulk suspension. We found throughout all of our simulations that the maximum in particle concentration can appear anywhere within the simulation cell, and that once formed, the cluster generally resides at the same horizontal position for the remainder of the simulation.

By summing the disturbance in velocity caused by all the particles in the suspension,

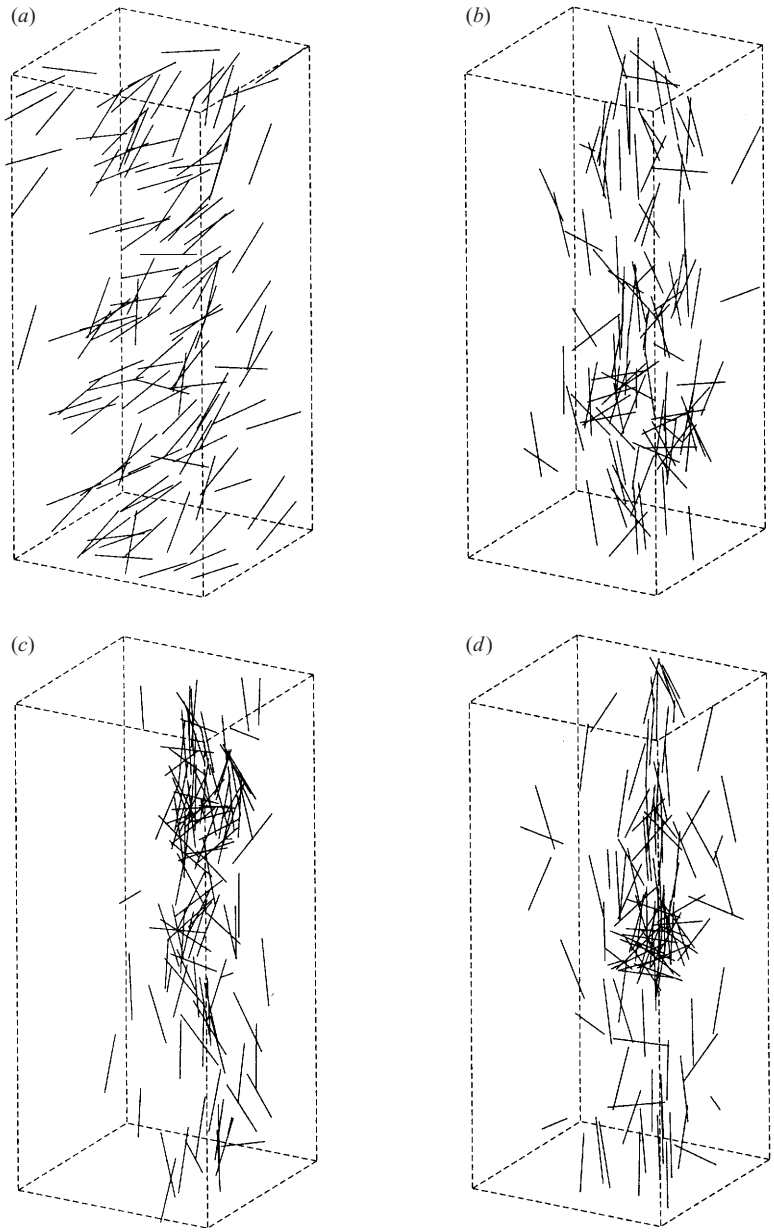

FIGURE 2. Plots of the suspension at (*a*) $t = 0$, (*b*) $t = 40.0$, (*c*) $t = 80.0$, and (*d*) $t = 120.0$. The simulation is for 128 particles with an average number density $nl^3 = 0.154$ and a fibre aspect ratio of $A = 11$. Gravity acts in the downward direction, lubrication was not included in this simulation, and the periodic cell has a height to width ratio of $d_z/d_w = 2$.

the fluid velocity at all positions within the periodic cell can be calculated. This was done for the data of figure 2 at $t = 120$ and then the vertical component of the velocity was averaged over the height of the cell to produce figure 3(*b*). (Velocities in the direction of gravity are defined as positive.) The position of highest velocity corresponds to the position of the cluster of particles. The fluid and particle velocities integrated over any plane of the cell must be zero to satisfy conservation

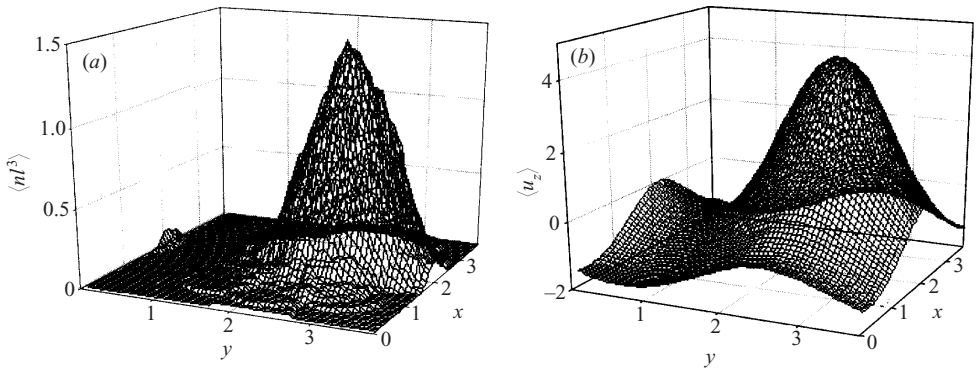

FIGURE 3. Vertically averaged number density (*a*) and fluid velocity (*b*) at $t = 120.0$ as a function of horizontal position for the case of 128 particles, no lubrication, $nl^3 = 0.154$, $A = 11$, and periodic cell ratio of $d_z/d_w = 2$.

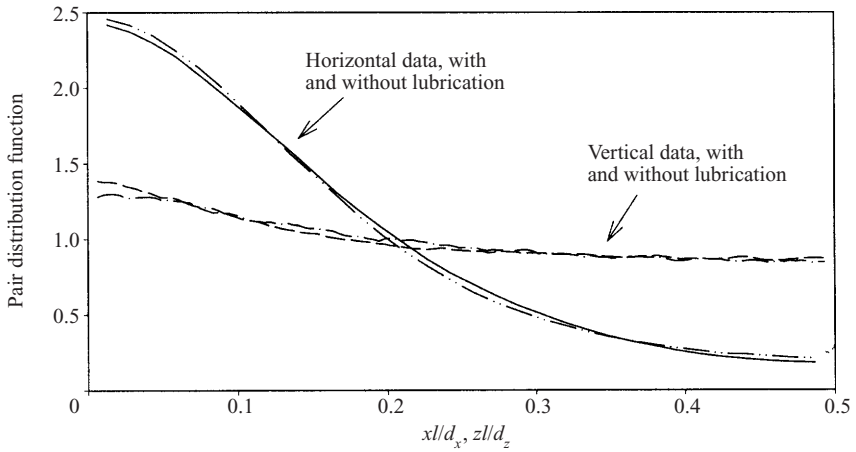

FIGURE 4. Comparison of the pair distribution function for the horizontal and vertical directions from simulations including and excluding lubrication. Computed for $A = 11$, $nl^3 = 0.154$, $N = 128$, and $d_z/d_w = 2$.

of volume; thus in regions where there are few particles the vertical fluid velocity is negative.

The pair distribution function provides a quantitative measure of the structure of the suspension. The pair probability at a specified distance is defined as the fraction of pairs of particles in the suspension having a centre-to-centre separation at that distance. The pair probabilities have been normalized to give the pair distribution function before being graphed in figure 4. The pair distributions have been split into horizontal and vertical components to clearly show that the cluster of particles is elongated in the direction of gravity. Note that only one cluster exists within the periodic box. Also, a comparison is made in figure 4 between simulations which included lubrication interactions and those that did not. For these conditions, excluding lubrication does not alter the spatial distribution of particles.

3.2. *Suspension sedimentation velocity*

Lubrication also has little influence on the average sedimentation velocity for the sedimentation of particles at an aspect ratio of $A = 11$ and number density of

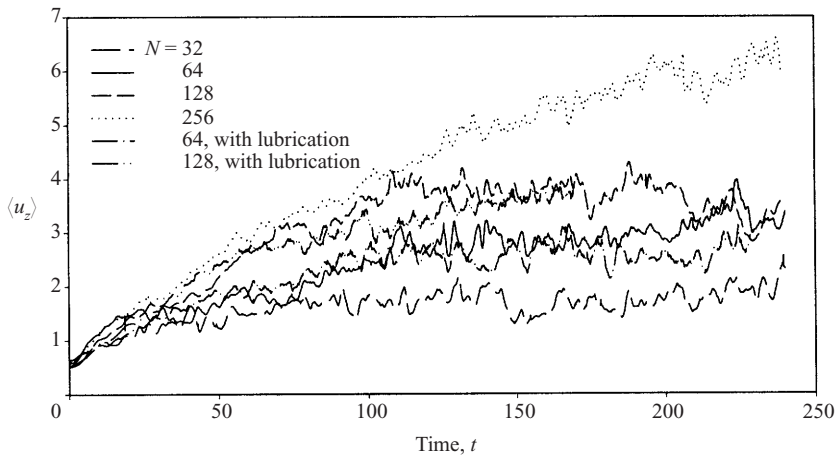

FIGURE 5. Average sedimentation rate as a function of time for varying number of particles within a simulation cell. Computed for $A = 11$, $nl^3 = 0.154$, $d_z/d_w = 2$.

$nl^3 = 0.154$. This is demonstrated in figure 5 which shows results for the sedimentation velocity from simulations with and without short-range interactions for $N = 64$ and 128. A comparison was not made for $N = 256$ particles for these conditions because the calculation with lubrication is very time consuming.

Figure 5 reveals that the steady sedimentation velocity varies as the number of particles in the simulation increases from $N = 32$ up to $N = 256$ at a fixed box ratio of $d_z/d_w = 2$. There is a linear increase in the sedimentation velocity with number of particles for simulations of 64 up to at least 256 particles. The increase in sedimentation velocity between $N = 32$ and 64 does not follow the same linear relationship; the increase is larger. In addition, the time to steady state also depends on the number of particles per periodic cell. For 32 particles, the suspension reaches steady state in a dimensionless time of approximately 75; for 256 particles, the sedimentation rate of the suspension does not equilibrate until $t \geqslant 200$.

For the calculations shown in figure 5, the height to width ratio of the periodic box was maintained at a constant value of $d_z/d_w = 2$. In order to double the number of particles, all dimensions of the cell were increased by a factor of $2^{1/3}$. As demonstrated next, the relative dimensions of the periodic cell also influence the average sedimentation velocity. By choosing a larger value of d_z/d_w, a sedimentation rate which converges with respect to the number of simulated particles can be calculated.

3.3. *Effect of periodic cell dimensions*

Stretching the simulation cell in the direction of gravity rather than increasing all dimensions proportionately gives a different behaviour for the average sedimentation velocity as a function of the number of simulated particles. The results in figure 6 demonstrate that the sedimentation velocity converges with particle number as long as only the height of the periodic box is increased, as opposed to the strategy of increasing all dimensions while keeping the box ratio constant as was done for the data of figure 5. For the simulations of figure 6, the horizontal dimensions of the periodic cell were held constant and the ratio of height to width was set equal to $N/16$. The simulations are for particles of aspect ratio 11 with no lubrication interactions and a suspension number density of $nl^3 = 0.154$. For $N = 128$ and $N = 256$, the

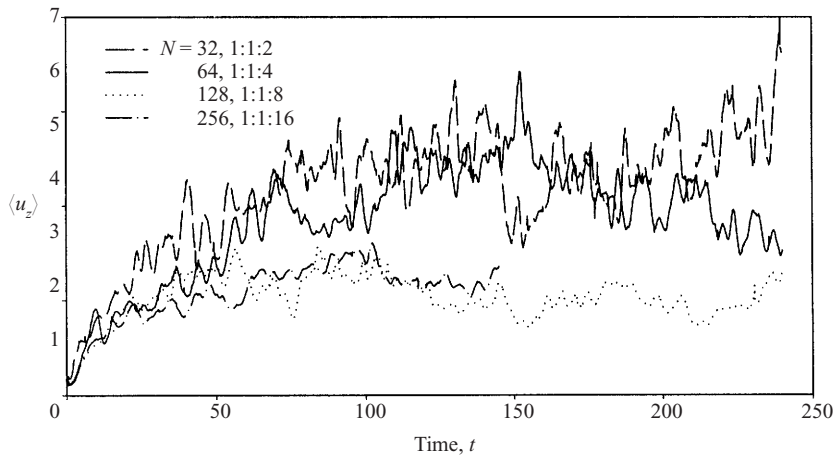

FIGURE 6. Sedimentation rate as a function of time for varying number of particles. The cell height is a function of the number of particles. Computed without using the lubrication approximations and with the parameters $A = 11$, $nl^3 = 0.154$, and $d_z/d_w = N/16$.

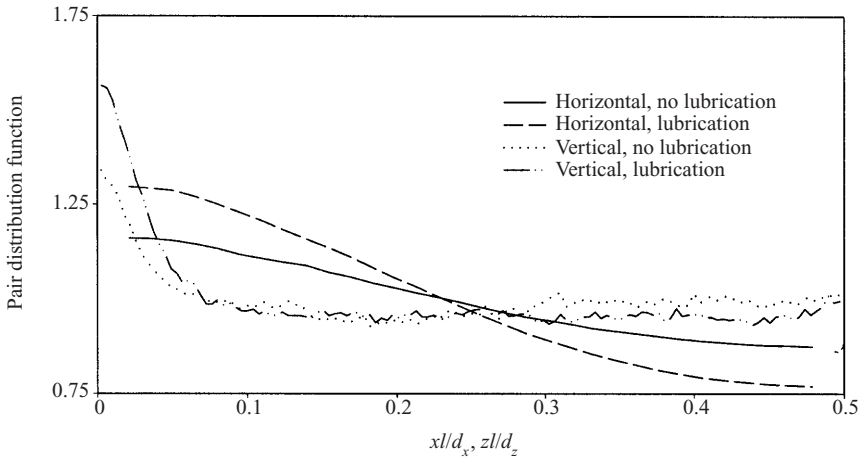

FIGURE 7. Time-averaged pair distribution functions for simulations with a periodic cell ratio of 8 to 1, $A = 11$, $nl^3 = 0.154$, and $N = 128$.

steady sedimentation rate is nearly identical. The simulation with 256 particles was stopped at $t = 150$ rather than $t = 240$ because of the large computational expense.

Due to the change in relative dimensions, there is now a small difference in the calculated sedimentation velocity which arises from including lubrication. Without lubrication the simulation gives a steady and convergent average sedimentation velocity of 1.03. With the lubrication interactions included, the value increases to 1.16. For number densities of 0.09 and 0.19, Herzhaft & Guazzelli (1999) measured sedimentation velocities of 1.08 ± 0.22 and 0.86 ± 0.14 respectively. (Note that the experimentally measured rates of sedimentation reported by Herzhaft & Guazzelli (1999) have been adjusted to account for the different non-dimensional velocity used in this paper.)

The difference in sedimentation rate which depends upon whether the simulation includes lubrication interactions arises from a corresponding difference in the structure

of the suspension. For the simulations including lubrication, the structure in the pair probabilities appears more pronounced in that the maximum in the pair probabilities is larger. As seen in figure 7, both the horizontal and vertical pair distribution functions are larger at small distances than the pair distribution functions for the simulations which did not include lubrication.

Notice that there are also differences in the pair probabilities of figure 7 compared to the previous results in figure 4 for the periodic box with dimensions $d_z/d_w = 2$. In simulations with the smaller cell ratio, the maximum in the pair distribution function for the horizontal direction was much greater than the maximum in the vertical direction. For the simulation cell with high aspect ratio, the maxima for the horizontal and vertical directions are of comparable value. The cluster of particles is still elongated in the gravitational direction, but is much more symmetric and has a clearly defined boundary in both the horizontal and vertical directions.

3.4. *Orientation distributions and dynamics*

Figure 8 shows the numerically calculated orientation distributions for a number density of $nl^3 = 0.05$ and fibre aspect ratio of $A = 11$ from simulations with periodic box ratios of $d_z/d_w = 2$ and 8. These results are from computations with $N = 128$ particles where the lubrication approximations were used. The orientation distribution from the experiments of Herzhaft & Guazzelli (1999) are also shown in figure 8 for the same number density and aspect ratio. The plots show the probability distribution of the fibres as a function of the projected angle, where the angle is measured with respect to the horizontal position. For the simulations, the orientation distribution depends upon the relative dimensions of the simulation cell. For a height to width ratio of 2, the simulations give a distribution of orientation which has a higher probability of alignment with the gravitational direction than for the simulations with $d_z/d_w = 8$.

Both the simulation results and the experimental observations indicate that the particles have a most probable orientation which is close to vertical. However, the simulations do not predict as large a probability for the particles to align with gravity as seen in the experiments. The experimental result indicates that the orientation distribution has two peaks: in addition to the maximum for orientations nearly in alignment with gravity, there is a slightly higher probability that a particle will align perpendicular to gravity rather than at an angle of $\pi/4$. The orientation distributions calculated from the simulation results indicate that the probability is roughly uniform from the horizontal orientation up to an angle of $\pi/4$, at which point the probability begins to increase.

The average change in alignment as a function of time is quantified in figure 9 for a suspension of fibres with an aspect ratio of $A = 11$ and bulk number density of $nl^3 = 0.154$. These simulations included lubrication. For each of the $N = 128$ fibres, the component of the orientation vector, $\boldsymbol{p}$, in the gravitational direction, p_3, is squared. Then an average over all the fibres is made and plotted versus time. The time for the orientation to reach a steady state is approximately the same, regardless of whether the value of the periodic cell ratio is 2 or 8. Once the fibre orientation reaches a steady state, the simulation with $d_z/d_w = 2$ clearly predicts a higher degree of average alignment in the direction of gravity than the simulation with a periodic cell ratio of $d_z/d_w = 8$.

After the average orientation for the fibres in the suspension reaches a steady state, the individual particles continue to change orientation. To quantify the dynamic changes in the orientation after attainment of steady state, autocorrelations for the

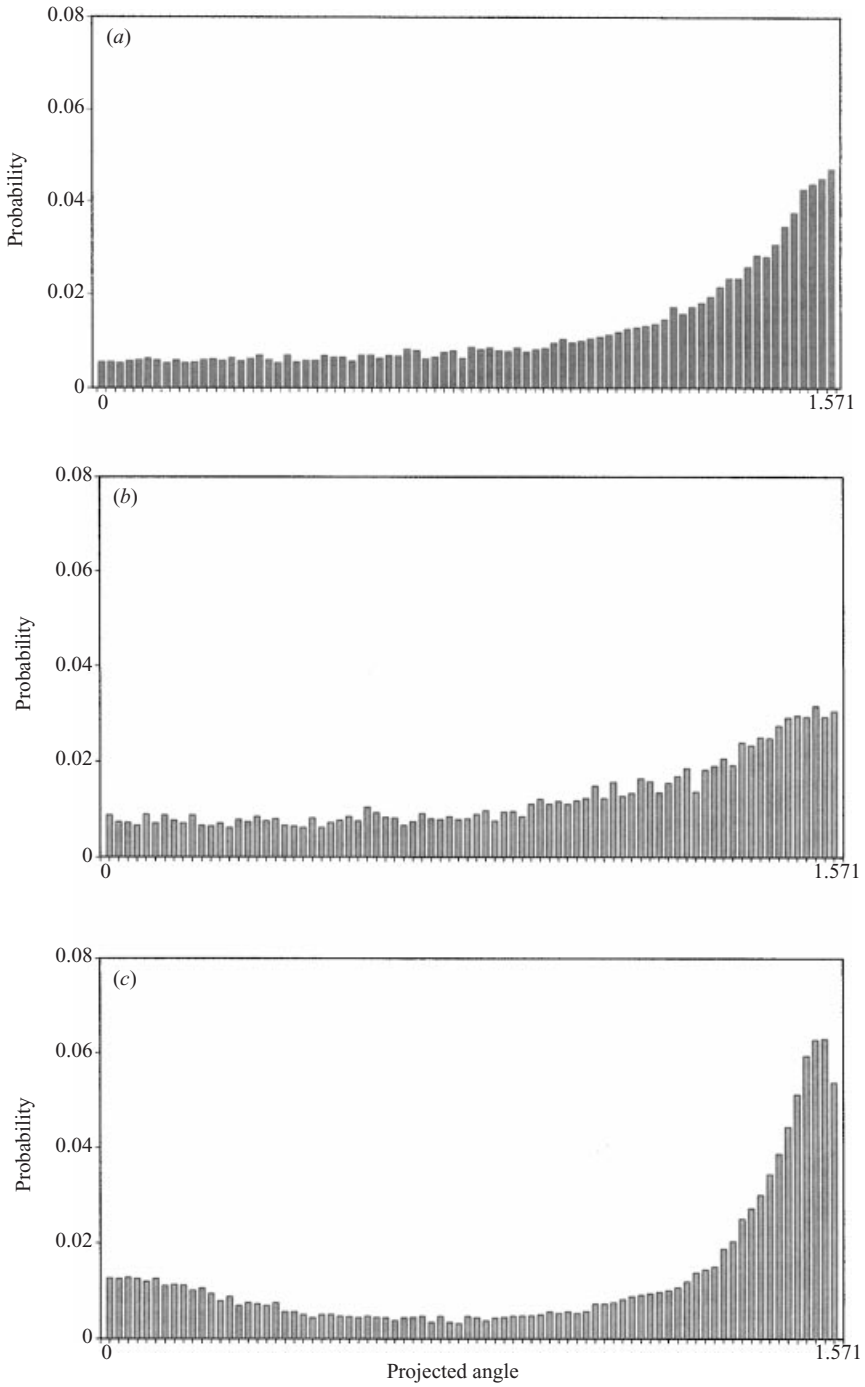

FIGURE 8. Comparison of orientation distributions for $A = 11$ and $nl^3 = 0.05$ from simulations and experiments of Herzhaft & Guazzelli (1999). Simulation results shown for calculations with lubrication and 128 particles for periodic box ratios of $d_z/d_w = 2$ (*a*) and $d_z/d_w = 8$ (*b*). Experimental measurements are displayed in (*c*).

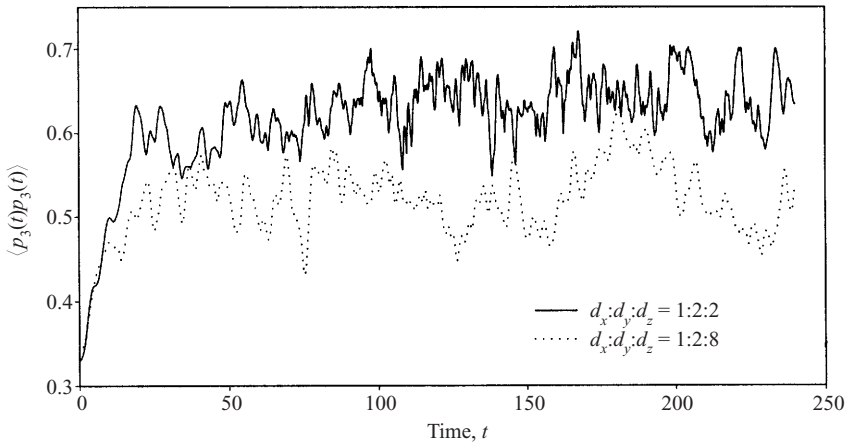

FIGURE 9. Time evolution of the average square orientation in the gravitational direction. Simulations for $N = 128$, $A = 11$, and $nl^3 = 0.154$ with lubrication and two different ratios of height to width for the periodic cell.

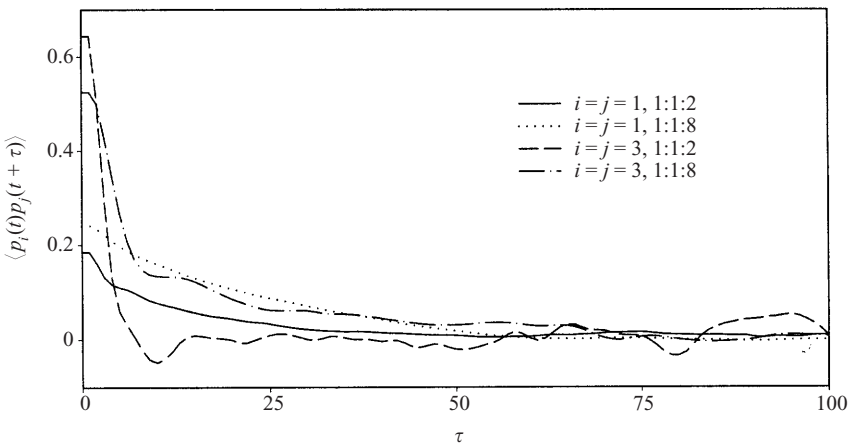

FIGURE 10. Autocorrelation function for the orientation. Simulations for $N = 128$, $A = 11$, and $nl^3 = 0.154$ with lubrication and two different ratios of height to width for the periodic cell.

orientations were calculated from the simulation data. Plots of both the vertical component of the autocorrelation, $\langle p_3(t)p_3(t+\tau)\rangle$, and one of the horizontal components of the autocorrelation function, $\langle p_1(t)p_1(t+\tau)\rangle$, are shown in figure 10 for values of t greater than the time to steady state. The vertical component of the orientation correlation decays rapidly for the simulation with a periodic box ratio of $d_z/d_w = 2$: the orientation becomes uncorrelated in a time of approximately $t = 15$. For $d_z/d_w = 8$, the component of the fibre orientation in the gravitational direction initially decays rapidly as does the simulation for $d_z/d_w = 2$, but for the case of $d_z/d_w = 8$ the decay slows before the orientation becomes uncorrelated at an approximate time of $t = 60$. The autocorrelation function for the horizontal component of the orientation decreases slowly at short and long times until becoming equal to zero at approximately $t = 60$ for both ratios of height to width for the periodic cell. Though the time at which the horizontal rotations decorrelate is approximately the same in the two simulation cells, the distance that a fibre must fall differs. For $d_z/d_w = 8$, the rotations

of the fibres become uncorrelated after an average fibre falls a distance of 35 fibre lengths at the average sedimentation rate of 1.16. In the simulation with $d_z/d_w = 2$, the average sedimentation velocity is over three times higher. Consequently, an average particle must fall a distance of 106 fibre lengths before the orientations become uncorrelated.

3.5. *Velocity distributions*

Figure 11 shows the velocity distribution of the fibres in suspension calculated for a number density of $nl^3 = 0.05$, fibre aspect ratio of 11, and $N = 128$. Results for the simulations with lubrication interactions and periodic box ratios of $d_z/d_w = 8$ and 2 are both included in the figure. The velocity distribution measured in experiments for the same number density and fibre aspect ratio is presented in figure 11(*c*). As expected, the horizontal velocities of the particles are distributed evenly about a velocity of zero for both the simulations and the experiments. The standard deviation, or velocity fluctuation of the fibres, for the horizontal direction is 0.20 ± 0.05 for the experiments and 0.16 for the simulations with $d_z/d_w = 8$. For $d_z/d_w = 2$, the horizontal fluctuations equal 0.22, which is larger than the value for the simulation with $d_z/d_w = 8$ and the experiment.

For the vertical velocities, the simulated distributions have significant differences which arise from the change in relative dimensions of the simulation cell. The fact that the sedimentation rate is larger for $d_z/d_w = 2$ has already been noted, but these plots also indicate that the distributions for vertical velocity for the two different box sizes are also very different. The fluctuations, or standard deviation, in the vertical velocity equal 0.6 for $d_z/d_w = 8$ and 1.7 when $d_z/d_w = 2$. A fibre can have a sedimentation velocity as high as 7.0 when the cell ratio equals 2. The maximum sedimentation rate for a fibre in the simulations with $d_z/d_w = 8$ is much closer to that observed in the experiments. The other aspects of the simulated distribution for $d_z/d_w = 8$ are also in closer agreement with the experimentally measured distribution. The average sedimentation velocity of the particles for the experiments is 0.79 ± 0.14, while the simulation predicts an average sedimentation velocity of 1.16. For $d_z/d_w = 8$, the velocity fluctuations of the fibres for the vertical direction are within one standard deviation of the velocity fluctuations observed in the experiments. The experimental measurement is 0.72 ± 0.14; the simulation gives a vertical velocity fluctuation of $\sigma_v = 0.60$. The experimental velocity distribution is nearly symmetric, whereas the simulation result with $d_z/d_w = 8$ predicts a slightly less symmetric distribution. The simulation accurately shows a long tail towards the higher velocities, but very few particles have a negative velocity.

The numerical data cited in the previous paragraph indicate that the shape of the periodic cell affects the fluctuations in velocity for the sedimenting fibres. Likewise, the box size also affects the calculated values of the velocity fluctuations. Figure 12 shows both the horizontal and vertical velocity fluctuations for $nl^3 = 0.154$, $A = 11$, and $d_z/d_w = 2$ as a function of number of simulated particles N, or the size of the periodic box. Notice that both the horizontal and vertical fluctuations increase linearly with N, though the horizontal fluctuations in velocity grow at a slower rate than the velocity fluctuations in the vertical direction. This phenomenon, unlike the problem with sedimentation velocity as seen in figure 5, is not unique to the sedimentation of rigid rods. Simulations of sedimenting suspensions of spherical particles using periodic boundary conditions exhibit very similar behaviour for the velocity fluctuations as a function of box size, as is explained in the work of Caflisch & Luke (1985) and Ladd (1997). The simulations of sedimenting suspensions of spheres indicate that the

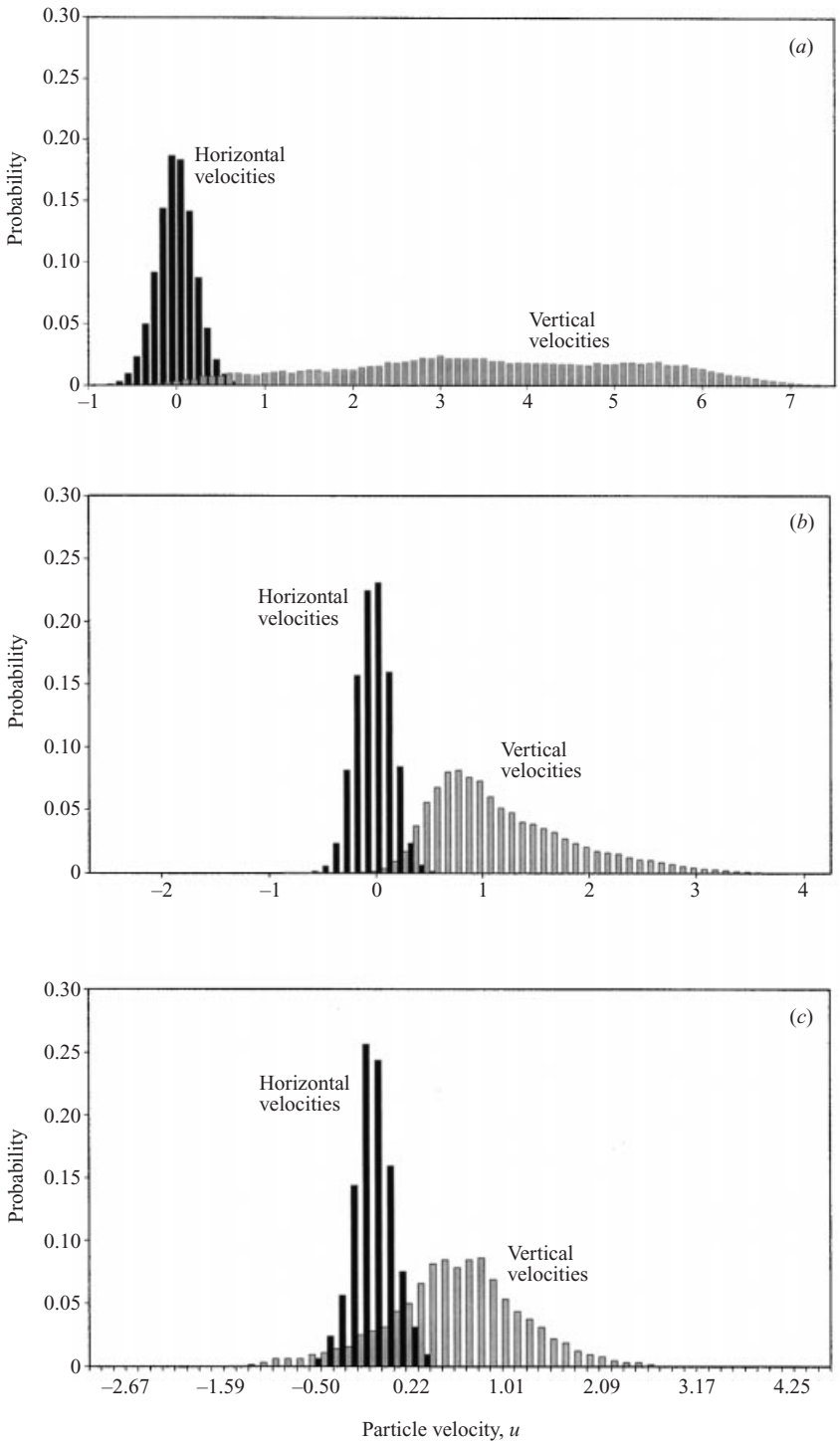

FIGURE 11. Comparison of velocity distributions for $A = 11$ and $nl^3 = 0.05$ from simulations and experiments of Herzhaft & Guazzelli (1999). Simulation results shown for calculations with lubrication and 128 particles for periodic box ratios of $d_z/d_w = 2$ (*a*) and $d_z/d_w = 8$ (*b*). Experimental measurements are displayed in (*c*).

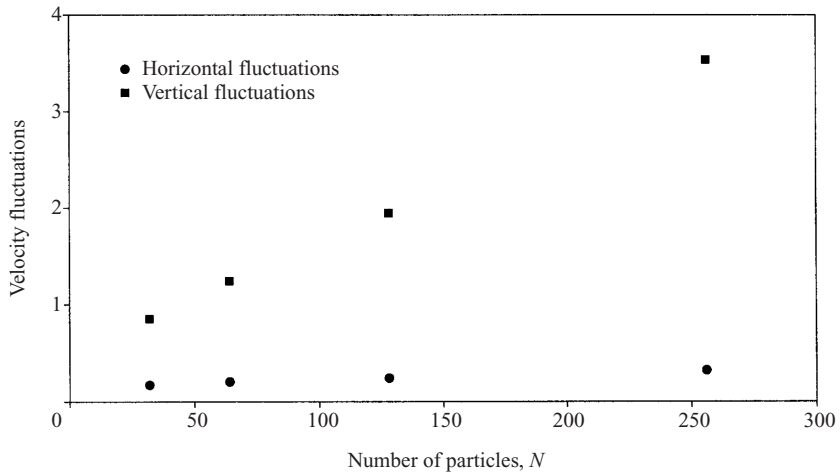

FIGURE 12. Horizontal and vertical velocity fluctuations as a function of the number of particles simulated. Simulation results shown for calculations without lubrication included and with $A = 11$, $nl^3 = 0.154$, and $d_z/d_w = 2$.

velocity fluctuations continue to diverge as N increases when using periodic boundary conditions.

3.6. *Concentration and aspect ratio dependence*

Up to this point, the simulations have been restricted to sedimenting suspensions of fibres with an aspect ratio of $A = 11$ and to only two values for the bulk number density. We now expand our investigation to include a fibre aspect ratio of 32 and a wider range of number densities.

Figure 13 displays average sedimentation rates for the suspension as a function of the concentration. The data shown in (*a*) are for an aspect ratio of 11, while the data in (*b*) are for an aspect ratio of 32. All the average sedimentation rates are from calculations with lubrication included and using $N = 128$ particles within a periodic box with a height to width ratio of $d_z/d_w = 8$. The data from experiments of Herzhaft & Guazzelli (1999) for the same fibre aspect ratios are also plotted, along with the estimates of error as reported by the authors. The simulated data have not been presented with error bars included. For most of the simulations, only a limited number of calculations were made owing to the computational expense. However, for $A = 11$ and $nl^3 = 0.019$ and 0.05, multiple runs were made and can be reported. For $nl^3 = 0.019$, the sedimentation velocity is 0.95 ± 0.08, and for $nl^3 = 0.05$, $\langle u_z \rangle_s s$ equals 1.16 ± 0.09. In both cases, the standard deviation is less than 10% of the mean value. Furthermore, the standard deviation of the mean value of the sedimentation rate is less than the fluctuation of the mean value for any one run. This indicates that the mean value, as calculated here with $N = 128$, is relatively insensitive to the initial configuration of the particles within the periodic cell.

For $A = 11$ and at low number densities, the average sedimentation velocities from the simulations agree closely with those measured in experiments as seen in figure 13(*a*). The sedimentation rate also exhibits a maximum between $nl^3 = 0.05$ and $nl^3 = 0.154$, which is observed in the experiments. The sedimentation rate predicted by the simulations is slightly higher than the experiments for $A = 32$. The velocities show the correct qualitative behaviour for values of $nl^3 < 1$, in that the velocity remains approximately constant. The simulations show a significant drop in the velocity at

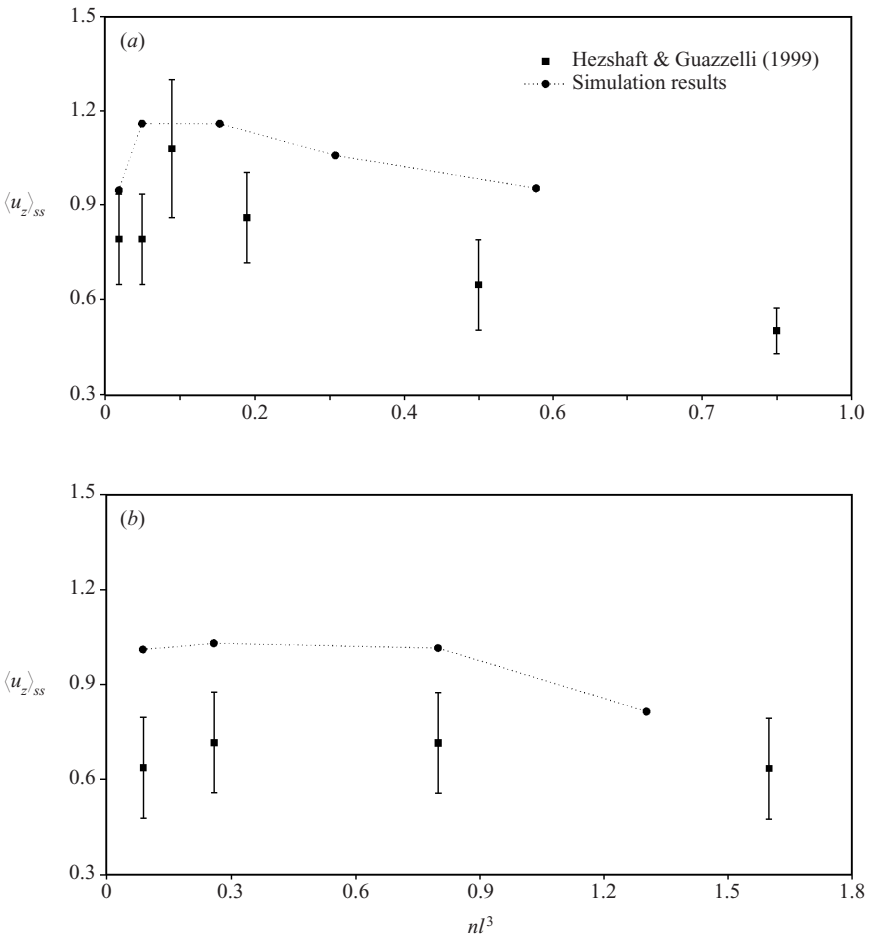

FIGURE 13. Average sedimentation rates at steady state as a function of number density nl^3. Results were calculated, with lubrication included, for $d_z/d_w = 8$ and $N = 128$ fibres with aspect ratios of $A = 11$ (a) and $A = 32$ (b). Simulation results are compared to the experimental measurements of Herzhaft & Guazzelli (1999).

$nl^3 = 1.305$; the sedimentation rate at this concentration is close in value to the rates measured in experiments at number densities of 0.8 and 1.6.

Figure 14 presents velocity fluctuations, or standard deviations in the velocities of the particles, corresponding to the average sedimentation rates of figure 13. At low number densities and for fibre aspect ratios of $A = 11$ and $A = 32$, both the horizontal and vertical velocity fluctuations agree quantitatively with those observed in experiments. However, the simulations predict that the fluctuations change very little as the average number density increases, whereas the experimentally measured fluctuations increase by a factor of up to two as the number density increases. The calculated ratios of the vertical to horizontal fluctuations in the particle velocities remain nearly constant at an approximate value of 3 over the entire range of number densities; this constant ratio of 3 agrees with the ratio reported by Herzhaft & Guazzelli (1999).

The simulation data graphed in figure 14 come from calculations with $d_z/d_w = 8$. For simulations with $d_z/d_w = 2$ the velocity fluctuations are larger. For a number

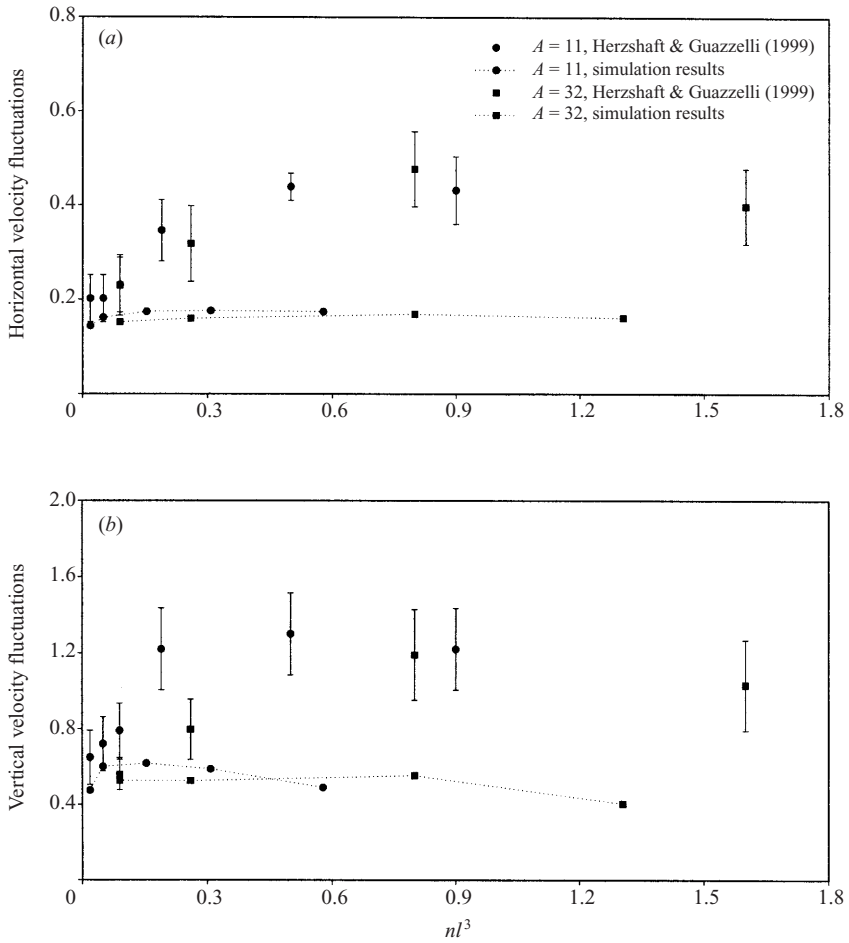

FIGURE 14. Velocity fluctuations as a function of number density. Results were calculated, with lubrication included, for $d_z/d_w = 8$ and $N = 128$ fibres with aspect ratios of $A = 11$ and $A = 32$. Horizontal components and vertical components are shown in (a) and (b), respectively.

density of $nl^3 = 0.154$, the horizontal fluctuation in the particle velocity equals 0.236 and 0.174 while the vertical fluctuation equals 1.74 and 0.617 for $d_z/d_w = 2$ and $d_z/d_w = 8$ respectively. At a lower number density of $nl^3 = 0.05$, the horizontal fluctuation for $d_z/d_w = 2$ is 1.4 times larger than the horizontal fluctuation when $d_z/d_w = 8$ and the vertical fluctuation is 2.8 times larger.

Figure 15 shows the orientation parameter as a function of nl^3 for aspect ratios of 11 and 32. These values are also from the calculations made with lubrication and using $N = 128$ particles within a periodic box with a height to width ratio of 8. The orientation parameter is an average measure of the orientation of the particles given by $\langle 2\cos^2(\phi) - 1\rangle$, where ϕ is the projected angle measured with respect to the horizontal direction and the brackets indicate an ensemble average over all the particles in the suspension. A value of 1 would indicate that all particles are aligned perpendicular to gravity while a value of -1 would indicate perfect alignment of all the fibres with gravity. The orientation parameter equals zero for a suspension of fibres with a randomized orientation.

The estimates of error for the experimentally measured orientation parameters are

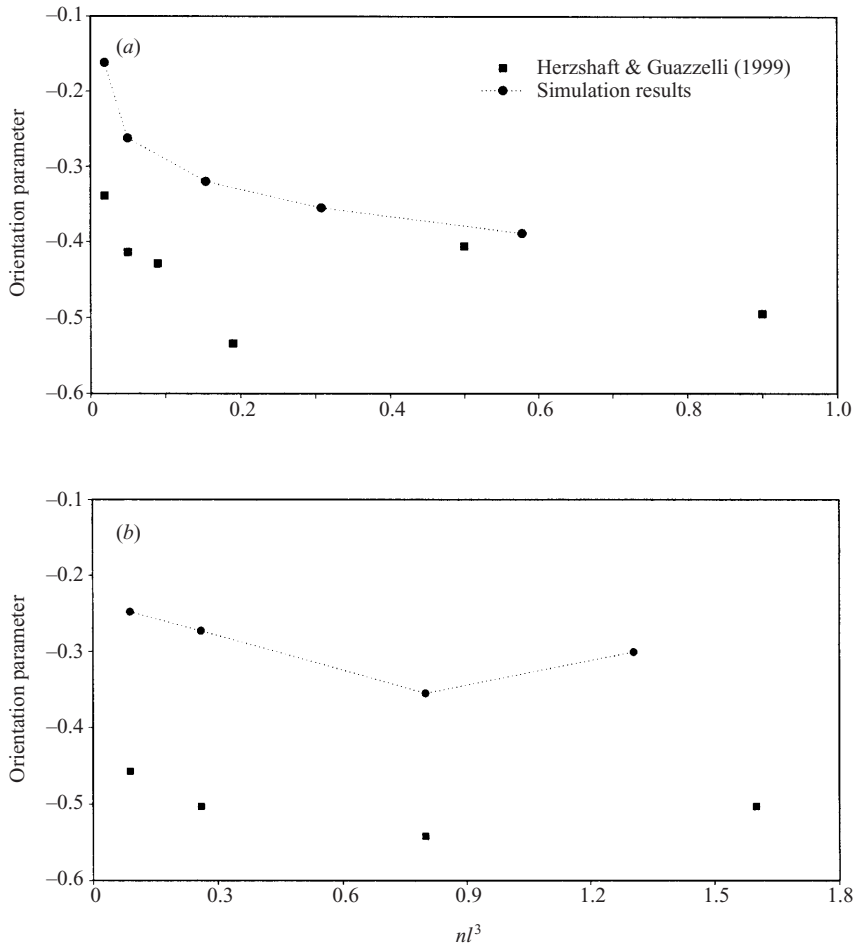

FIGURE 15. Orientation parameters at steady state as a function of number density nl^3. Results were calculated, with lubrication included, for $d_z/d_w = 8$ and $N = 128$ fibres with aspect ratios of $A = 11$ (*a*) and $A = 32$ (*b*). Simulation results are compared to the experimental measurements of Herzhaft & Guazzelli (1999).

not shown on the graphs in figure 15 since they are small in comparison to the size of the point; Herzhaft & Guazzelli (1999) report errors which are no larger than 1.5% of the value of the orientation parameter. As with the sedimentation velocity, the error in the orientation parameter was estimated for the cases of the lowest two number densities at an aspect ratio of $A = 11$. For $nl^3 = 0.019$, the orientation value was found to have an average value of -0.14 and a standard deviation of 0.01. For the case of $nl^3 = 0.05$, the orientation parameter equals -0.26 ± 0.02.

Both the simulations and experiments indicate that particles tend to align with gravity. However, figure 15 demonstrates that the simulations consistently predict a smaller degree of alignment than the experiments when $d_z/d_w = 8$. This fact can also be observed in the comparison of orientation distributions between the simulations and experiments for $nl^3 = 0.05$ and $A = 11$ as seen in figure 8. For simulations using a periodic cell ratio of $d_z/d_w = 2$, the orientation parameter is more negative, and thus agrees with the experiments better. At $nl^3 = 0.05$ and $nl^3 = 0.154$, the orientation parameter calculated by simulations with $d_z/d_w = 2$ equals -0.44 and

−0.49. At $nl^3 = 0.05$, the experimentally measured value equals −0.41. At number densities of $nl^3 = 0.09$ and 0.19, the measured values are −0.43 and −0.53. Despite the fact that the orientation parameters are in better agreement, there are still some important differences in the distribution of orientation for $d_z/d_w = 2$ as seen in figure 8. Some possible origins of the discrepancy in the orientation parameter between the simulations with $d_z/d_w = 8$ and the experimental observations are discussed in the following section along with a discussion of the other results.

4. Discussion

The simulation results from the preceding section represent a significant improvement over earlier attempts to numerically calculate the sedimentation of rigid fibres in suspension in the limit of zero Reynolds number. In addition, these results confirm the essence of existing theory and experiments. We discuss each of these assertions in turn.

4.1. *Steady and convergent sedimentation velocities*

Compared to previous simulations, perhaps the most striking achievement of this method is its ability to calculate a steady sedimentation velocity. The dynamic simulations of Mackaplow & Shaqfeh (1998) did not allow for calculation of a steady-state sedimentation velocity. Rather, the point particles used in those simulations formed a cluster which became increasingly dense as time progressed, and the fibres in the suspension never attained a steady, average structure. Thus the sedimentation velocity increased indefinitely.

The current simulation method demonstrates that a finite, steady sedimentation rate can be calculated by distributing the effects of hydrodynamic interactions along the entire length of the fibre as opposed to concentrating them at a point. Furthermore, calculating a steady sedimentation velocity does not depend on including lubrication interactions within the algorithm. Indeed, many of the simulation results indicate that lubrication interactions have a marginal impact on the solution for small number densities, though the short-range interactions become increasingly important as the number density exceeds $nl^3 = 0.2$.

The simulation successfully predicts a steady sedimentation velocity, but we have also found that calculating a convergent velocity requires selecting the proper ratio of height to width for the dimensions of the periodic cell. As seen in figure 6, the velocity converges as the number of particles increases if the periodic cell height is increased in a direct one-to-one proportion with the number of particles.

When all dimensions are increased as the number of particles increases, the sedimentation rate grows linearly as a function of the number of particles (see figure 5). The particle cluster in these simulations is highly concentrated in the horizontal directions, but is relatively uniform in the vertical direction. This column of particles, which spans the height of the periodic cell, convects downward with resistance provided primarily by the fluid shear at the boundary between the highly concentrated region and the clarified fluid. This structure and related sedimentation velocity clearly do not represent the observations made in experiments.

Increasing the length of the periodic cell in the direction of gravity changes the structure of the suspension. Figure 7 shows that the maximum in the pair distribution function in the vertical direction is comparable to that in the horizontal direction; the cluster is slightly elongated in the gravity direction, but is otherwise symmetric. The leading edge of the concentrated region of particles must overcome the strong

resistance associated with falling through a volume of clarified fluid, much like an isolated cluster of particles in an infinite fluid would. As highlighted next in our discussion, these simulations accurately reproduce the major features observed in experiments for the sedimentation velocity as a function of number density and aspect ratio.

4.2. *Comparison of velocity data with experiments*

The formation of particle clusters during the sedimentation of the suspension of rigid fibres causes an enhanced sedimentation rate at low number densities. For the range of number densities and aspect ratios studied, the sedimentation velocity at steady state is higher than expected for a spatially homogeneous suspension with the same orientation distribution. For some conditions, the suspension of particles sediments more rapidly than a single, isolated fibre aligned with gravity.

The comparisons with experiments shown in figure 13 for $A = 11$ and $A = 32$ demonstrate that the simulation is predicting accurate results for the particle sedimentation rates. For $A = 11$, the simulation and experimental results agree quantitatively at low number densities. For $A = 32$ and low number densities, the calculated rates are slightly higher than the rates observed in experiments. However, for the lower number densities, the simulations are in qualitative agreement with the experiments. Also, the calculated sedimentation rate at a number density of $nl^3 = 1.3$ is within one standard deviation of the sedimentation velocities measured at the two closest values of the number density of the suspension.

The comparisons of the calculated sedimentation velocities with the experiments may be better than they appear. The error bars in figure 13 show the standard deviation in the measurement of the average sedimentation velocity. However, there are additional errors present in the experiments that have an impact on the measured sedimentation rate which are not reflected in the experimental errors shown in figure 13. For example, Herzhaft & Guazzelli (1999) report significant errors for parameters such as the bulk number density and the fibre aspect ratio.

The experimental results show that the sedimentation rate of the fibres increases and then decreases as the average value of the number density increases. This maximum is particularly apparent in the data for fibres of aspect ratio 11, but also exists for the fibres of aspect ratio 32. The simulations accurately predict the maximum in sedimentation velocity and demonstrate that this maximum is caused by changes in the structure and orientation distribution of the suspension as the bulk number density changes. Figure 16 shows the horizontal component of the pair distribution function for the lowest and highest number densities which were simulated for a fibre aspect ratio of $A = 11$. These two distributions are nearly identical and figure 13 indicates that the sedimentation velocities are approximately the same. For randomly oriented suspension of rods which have the same pair distribution, the suspension of higher concentration at $nl^3 = 0.578$ should have a lower sedimentation rate than the suspension at $nl^3 = 0.019$ due to the increased hindrance of sedimentation at higher volume fractions which arises from the fluid back-flow. However, orientation plays a role in determining the sedimentation rate of the suspensions, and figure 15 shows that the particles are more aligned with the gravitational direction for the case of $nl^3 = 0.578$. This higher alignment allows the suspension to sediment as fast as the suspension of lower number density which has a similar pair distribution function.

Figure 16 also shows the horizontal component of the pair distribution function for $nl^3 = 0.154$, which is close to the average number density at which the sedimentation rate attains its maximum value. At this number density, the pair distribution function

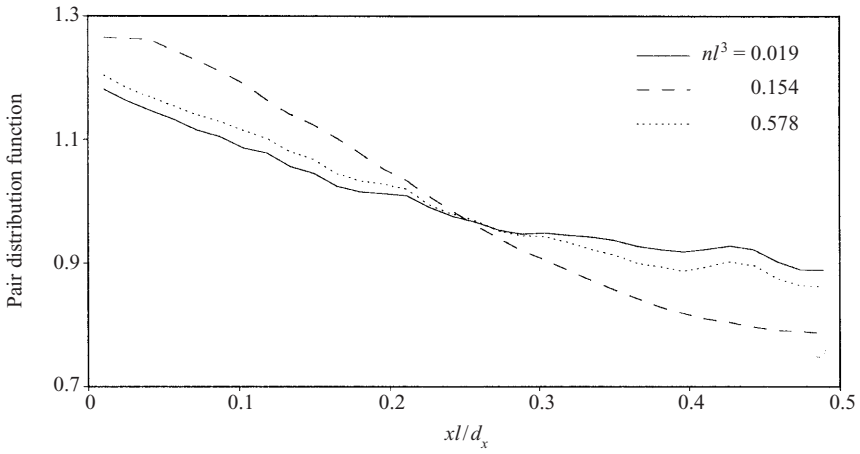

FIGURE 16. Comparison of the pair distribution function in the horizontal direction for three average number densities. Calculations with lubrication for $A = 11$, $N = 128$, and $d_z/d_w = 8$.

has a higher gradient than the pair distribution functions from the lower concentration at $nl^3 = 0.019$ and the higher concentration at $nl^3 = 0.578$. The higher gradient along with the fact that the volume fraction is lower ensures that the sedimentation velocity at $nl^3 = 0.154$ is higher than at $nl^3 = 0.578$ despite the fact that the degree of orientation with gravity is slightly higher at $nl^3 = 0.578$. Compared to sedimentation at an average number density of $nl^3 = 0.019$, the higher gradient of the pair distribution function together with the higher probability of orientation of a fibre with gravity at $nl^3 = 0.154$ results in a larger sedimentation rate even though the average number density is bigger. Thus the sedimentation velocity of the fibres has a maximum due to a combination of the changes in the structure of the suspension and the average orientation of the fibres in the suspension.

Figure 11 demonstrates that the particle velocity distributions from the simulation results with $d_z/d_w = 8$ and experimental observations of Herzhaft & Guazzelli (1999) are in good agreement at a bulk number density of $nl^3 = 0.05$ and fibre aspect ratio of $A = 11$. The simulations predict that few particles have a negative sedimentation velocity at any given point in time after the average quantities of the suspension attain a steady state. However, the experiments indicate that a significant fraction of particles in the suspension have a sedimentation velocity which is negative.

A related problem is that of the velocity fluctuations shown in figure 14. The calculated values of the velocity fluctuations for the sedimenting particles quantitatively agree with the experimentally measured fluctuations for both aspect ratios of $A = 11$ and 32 as long as the bulk number density is lower than 0.1. Also, the calculated ratio of the vertical to horizontal fluctuations remains nearly constant over the entire range of concentrations at a value of 3 as observed in the experiments. However, the velocity fluctuations do not increase as the number density increases as seen in the experimental measurements.

The better agreement between the simulations and experiments for the velocity fluctuations calculated at low, as opposed to high, number densities suggests that the algorithm may not be accurately accounting for the hydrodynamic interactions at higher number densities. Our simulation algorithm contains some inherent assumptions which might be responsible. First, the slender-body theory of Batchelor (1970) models a particle of very high aspect ratio, whereas these simulations are for

fibres of moderately high aspect ratios. Also, the force distribution on each particle includes only the linear terms as seen in equation (2.13). Retaining terms of higher order in the expansion of the force distribution could noticeably alter the results of the calculations at high number densities. We have also made some simplifying approximations when calculating the lubrication interactions between pairs of fibres.

The periodic boundary conditions are another possible source of error in the calculation of the velocity fluctuations shown in figure 14 at the higher number densities. Increasing the average number density while keeping the number of particles, N, constant at 128 lowers the size of the periodic box and the separation distances between the neighbouring images of a particle. Since the periodic cell is elongated in the vertical direction for the data presented in figure 14, the horizontal dimension of the periodic cell becomes critically small at the higher number densities. For example, the ratio of cell width in the horizontal direction to fibre length (as given by $d_w/2$, since d_w is the width of the periodic cell as non-dimensionalized by the fibre half-length) is 4.72 at the lowest average number density used in the simulations with a fibre aspect ratio of $A = 11$. At the highest concentration of $nl^3 = 0.578$, the ratio $d_w/2$ equals 1.5, indicating a separation of one half-length between the tips of neighbouring particles having a horizontal orientation which is aligned with the edge of the periodic cell. For an aspect ratio of $A = 32$ and number density of $nl^3 = 1.305$, the ratio $d_w/2$ has a value of 1.15. For all of the simulations, therefore, the fibres are free to rotate without colliding with their nearest neighbouring images. However, the close spacing between the neighbouring images of fibres which exists at the higher number densities may be altering the dynamics of the particles.

4.3. *Comparison of orientation results with experiments*

The simulation results confirm the experimental observation that the fibres in the suspension preferentially align with gravity during the sedimentation process. This alignment of the rigid fibres is induced by the average flow field which results from the formation of clusters of particles. The downward convection of a cluster of particles creates a shear gradient between the regions of high and low concentration. This gradient in the average flow velocity is plotted in figure 3 which shows the average concentration and vertical velocity of the fluid as a function of horizontal position for the case of $nl^3 = 0.154$, $A = 11$, $N = 128$, and $d_z/d_w = 2$. This fluid shear gradient tends to align particles in the gravitational direction, much like a rigid fibre of infinite aspect ratio aligns with the flow direction in a simple shear flow.

The simulation results shown in figure 15 predict a smooth functional relationship between the orientation parameter and nl^3, but in the text of their paper, Herzhaft & Guazzelli (1999) claim that there is no trend in the orientation parameter. However, the simulations indicate a trend with which the experimental data qualitatively agree. At small number densities for $A = 11$ and $A = 32$, the orientation parameter decreases, more distinctly for the $A = 11$ case. Also for $A = 11$, the simulations indicate that the orientation parameter is quickly approaching zero as the bulk number density goes to zero, which is expected. At high number densities and for $A = 11$, the orientation parameter appears to approach a constant value for the simulations. Except for the point at $nl^3 = 0.5$, the experimental values appear to do the same. For $A = 32$, the orientation parameter increases slightly for the highest number density plotted for both the simulation and experiment.

Although the simulations predict that the fibres preferentially align with gravity, the steady and convergent simulation results of figure 15 indicate that the sedimenting

fibres do not align with gravity to as high a degree as the fibres observed in the experiments for the same aspect ratio and number density. This fact is also evident in the plots of orientation distribution as seen in figure 8. The origins of the difference can possibly be attributed to the same reasons listed above for the lack of agreement in the velocity fluctuations between the simulations and experiments. The possibilities include errors resulting from approximations of the hydrodynamic interactions between particles and the issues arising from the periodic boundary conditions.

Besides the fact that the simulations are under predicting the degree of alignment, the results also indicate that changing the ratio of height to width for the periodic cell affects the orientation of the particles in the simulated suspension. The slower decay of the autocorrelation function of the orientation for the vertical direction (figure 10) and the lower degree of alignment with gravity (figure 8 and figure 9) for the fibres in the simulation cell of aspect ratio $d_z/d_w = 8$ can both be attributed to the difference in the structure of the suspension and the resulting velocity field. As already discussed in relation to the average sedimentation velocity, the particles in the periodic box with a height to width ratio of 2 are arranged in a cluster which is highly concentrated in the horizontal direction. This highly concentrated cluster creates the strong shear flow seen in figure 3 which acts to align the particles. For the periodic cell with the higher ratio of $d_z/d_w = 8$, the cluster of particles is not as concentrated and the resulting difference in velocity between concentrated and non-concentrated regions is smaller. Consequently, the flow field does not align the particles as strongly and does not mix the vertical component of the orientations as rapidly.

Extending the periodic cell in the gravitational direction enables calculation of a convergent value for the sedimentation velocity by changing the microstructure of the suspension, as argued in § 4.1. Unfortunately, as described in the previous paragraph, the change in structure also has a detrimental impact upon the orientation distribution. This suggests that the particle microstructure is probably still not a fully accurate representation of the structure which exists in the experiments. Of course, as discussed in § 4.2, the structure is highly confined in the horizontal direction, since the periodic cell has a relatively small width. If the horizontal dimension of the periodic cell could be increased while holding the height constant, the problem with the orientation distribution might be corrected. However, testing this idea requires performing simulations which have a significantly larger number of particles than $N = 128$.

Whether the ratio of height to width for the periodic box equals 2 or 8, the vertical component of the autocorrelation function decreases more rapidly than the horizontal component at short times. This can be explained by once again referring to the average flow field which is plotted in figure 3 for the case of $d_z/d_w = 8$. As fibres flow into and out of the cluster, they must cross a region of high shear caused by the difference in average vertical velocity between the cluster and clarified fluid. A fibre with a centre-of-mass position near this region of high shear will preferentially align with gravity, but the alignment will experience small fluctuations. If the fluctuations tilt the end of the fibre pointing in the gravitational direction away from the region of concentrated particles where the sedimentation velocity is relatively high, the particle will rapidly flip. During the vertical rotation, the fibre remains oriented in the plane of shear with the horizontal projection of the orientation vector always pointing toward or away from the region of high concentration. This flipping of particles due to the shear gradient in the sedimenting suspension causes the autocorrelation of the vertical orientation to decay rapidly. A similar mechanism which would quickly decorrelate the horizontal components of orientation of the fibres does not exist.

4.4. *Structure of the suspension*

The stability calculations made by Koch & Shaqfeh (1989) predict a horizontal spacing of $(nl)^{-1/2}$ between regions of high particle density. Unfortunately, in these simulations only one cluster of particles forms in each periodic cell, so we are unable to confirm the predicted scaling. Also, the relative dimensions of the periodic box control the detailed structure of the suspension as seen in the comparison of the pair distribution functions between figure 4 and figure 7. The other properties of the suspension also change as a consequence of the alterations in the structure. Using a ratio for the periodic box of $d_z/d_w = 8$ rather than $d_z/d_w = 2$ enables the calculation of convergent sedimentation velocities which agree very closely with those measured in the experiments. Some of the other properties of the sedimenting suspension do not change as favourably. For example, the error between the simulation and experimental results for the orientation parameter increased upon elongating the periodic box and we have argued that this is directly due to the alteration in the suspension structure.

The maximum number of particles used in the calculations is 256, and most of the results are for $N = 128$. Increasing the size of the simulation significantly beyond 256 particles may allow for the formation of multiple clusters in each periodic cell and remove the strong dependence upon the relative dimensions of the periodic cell. However, this is not absolutely clear; the dependence of the structure of the suspension could arise from either the small size of the simulation or possibly the periodic boundary conditions themselves.

Since we cite the dependence of the structure of the simulated suspension on the relative dimensions of the periodic cell as a possible source of most of the discrepancies between these simulations and the experimental measurements, a direct comparison with the structure observed in the experiments is desirable. Unfortunately, an experimental measurement of the structure of the suspension during sedimentation has not been made. Both Herzhaft *et al.* (1996) and Herzhaft & Guazzelli (1999) published images of the sedimenting fibres which clearly indicate the presence of fibre clusters, but a quantitative analysis of the structure of the suspension was not attempted in either study. Most specifically, the size and the anisotropy of the clusters of particles in addition to the spacing between the clusters is not known; a measurement of the pair distribution function would be ideal since it would contain all of this information. Additionally, an experimental measurement of the suspension structure would enable a valuable comparison to the horizontal spacing between clusters of $(nl)^{-1/2}$ which is predicted by the theoretical calculations of Koch & Shaqfeh (1989).

5. Conclusions

In agreement with theoretical calculations and experiments, these simulations demonstrate that a suspension of rigid fibres can become heterogeneous during sedimentation. The instability which causes the demixing of the fibres during the sedimentation process arises purely from hydrodynamic interactions between the particles. For some simulations, a small and short-ranged irreversible force was included to assist in maintaining the excluded volume of the particles, but this force was found to play no role in the instability.

The effect of the instability is readily apparent from direct visualizations of the simulations which show that some regions of the periodic simulation cell contain clusters of particles whereas other regions have a deficit of particles. We have quanti-

fied the structure of the suspension by calculating the pair distribution function. The result clearly demonstrates the existence of a non-uniformity in the relative positions of the centres of mass for pairs of fibres in the suspension. The pair distribution function also has an anisotropic solution which reflects the elongation of the cluster of particles in the direction of gravity.

For the first time, we have calculated via computer simulation a steady and convergent sedimentation velocity for a suspension of rigid fibres sedimenting in the limit of zero Reynolds number. The average sedimentation velocities agree closely with those observed in the experiments of Herzhaft & Guazzelli (1999) for the range of aspect ratios and number densities used in the calculations. This agreement includes the accurate prediction of the simulations that a maximum exists in the average sedimentation velocity as a function of the average number density. Furthermore, the calculations demonstrate that the formation of particle clusters due to the hydrodynamic instability can cause the sedimentation rate of a suspension of rigid fibres to exceed the maximum rate of sedimentation for an isolated fibre in an infinite fluid.

The simulation results confirm the experimental observations of Herzhaft & Guazzelli (1999) that fibres in suspension tend to align with gravity during sedimentation. The average orientations from the simulations were compared to the experiments and found to be in qualitative agreement. The degree of alignment with the gravitational direction, though, was consistently lower than that seen in the experiments for the aspect ratios and number densities which were simulated. In addition to comparing the average particle orientations, we have compared the calculated orientation distributions with experimental results and have reported on the dynamic changes in orientation of the particles.

The fact that the sedimentation of suspensions of non-colloidal, rigid fibres is unstable and that the instability can induce an inhomogeneous distribution of particles and an enhanced sedimentation velocity is now well established. The supporting research includes the original theoretical calculations of Koch & Shaqfeh (1989), the experimental work of Herzhaft *et al.* (1996) and Herzhaft & Guazzelli (1999), and the simulation results presented within this paper.

We thank Dr Donald L. Koch and Dr Elisabeth Guazzelli for their suggestions and comments on this work. This research project was supported by a grant from the Petroleum Research Fund of the American Chemical Society.

REFERENCES

Batchelor, G. K. 1970 Slender-body theory for particles of arbitrary cross-section in Stokes flow. *J. Fluid Mech.* **44**, 419–440.

Brady, J. F. & Bossis, G. 1988 Stokesian Dynamics. *Annu. Rev. Fluid Mech.* **20**, 111–157.

Caflisch, R. E. & Luke, J. H. C. 1985 Variance in the sedimentation speed of a suspension. *Phys. Fluids* **28**, 759–760.

Chwang, A. T. & Wu, T. Y. 1974 Hydromechanics of low-Reynolds-number flow. Part 1. Rotation of axisymmetric prolate bodies. *J. Fluid Mech.* **63**, 607–622.

Chwang, A. T. & Wu, T. Y. 1975 Hydromechanics of low-Reynolds-number flow. Part 2. Singularity method for Stokes flows. *J. Fluid Mech.* **67**, 787–815.

Claeys, I. L. & Brady, J. F. 1989 Lubrication singularities of the grand resistance tensor for two arbitrary particles. *Physico Chem. Hydrodyn.* **11**, 261–293.

Claeys, I. L. & Brady, J. F. 1993*a* Suspensions of prolate spheroids in Stokes flow. Part 1. Dynamics of a finite number of particles in an unbounded fluid. *J. Fluid Mech.* **251**, 411–442.

Claeys, I. L. & Brady, J. F. 1993*b* Suspensions of prolate spheroids in Stokes flow. Part 2. Statistically homogeneous dispersions. *J. Fluid Mech.* **251**, 443–477.

Claeys, I. L. & Brady, J. F. 1993*c* Suspensions of prolate spheroids in Stokes flow. Part 3. Hydrodynamic transport properties of crystalline dispersions. *J. Fluid Mech.* **251**, 479–493.

Durlufsky, L. J. & Brady, J. F. 1989 Dynamic simulation of bounded suspensions of hydrodynamically interacting particles. *J. Fluid Mech.* **200**, 39–67.

Durlofsky, L. J., Brady, J. F. & Bossis, G. 1987 Dynamic simulation of hydrodynamically interacting particles. *J. Fluid Mech.* **180**, 21–49.

Fan, X., Phan-Thien, N. & Zheng, R. 1998 A direct simulation of fiber suspensions. *J. Non-Newtonian Fluid Mech.* **74**, 113–135.

Harlen, O. G., Sundararajakumar, R. R. & Koch, D. L. 1999 Numerical simulation of a sphere settling through a suspension of neutrally buoyant fibres. *J. Fluid Mech.* **388**, 355–388.

Hasimoto, H. 1959 On the periodic fundamental solutions of the Stokes equations and their application to viscous flow past a cubic array of spheres. *J. Fluid Mech.* **5**, 317–328.

Herzhaft, B. & Guazzelli, E. 1999 Experimental study of the sedimentation of dilute and semi-dilute suspensions of fibres. *J. Fluid Mech.* **384**, 133–158.

Herzhaft, B., Guazzelli, E., Mackaplow, M. B. & Shaqfeh, E. S. G. 1996 Experimental investigation of the sedimentation of a dilute fiber suspension. *Phys. Rev. Lett.* **77**, 290–293.

Höfler, K. & Schwarzer, S. 2000 Navier–Stokes simulation with constraint forces: Finite-difference method for particle-laden flows and complex geometries. *Phys. Rev.* E **61**, 7148–7160.

Kim, S. & Karrila, S. P. 1991 *Microhydrodynamics: Principles and Selected Applications.* Butterworth-Heinemann.

Koch, D. L. & Shaqfeh, E. S. G. 1989 The instability of a dispersion of sedimenting spheroids. *J. Fluid Mech.* **209**, 521–542.

Kuusela, E., Höfler, K. & Schwarzer, S. 2001 Computation of particle settling speed and orientation distribution in suspensions of prolate spheroids. *J. Engng Maths* **41**, 221–235.

Ladd, A. J. C. 1997 Sedimentation of homogeneous suspensions of non-Brownian spheres. *Phys. Fluids* **9**, 491–499.

Mackaplow, M. B. & Shaqfeh, E. S. G. 1998 A numerical study of the sedimentation of fiber suspensions. *J. Fluid Mech.* **376**, 149–182.

Turney, M. A., Cheung, M. K., Powell, R. L. & McCarthy, M. J. 1995 Hindered settling of rod-like particles measured with magnetic resonance imaging. *AIChE J.* **41**, 251–257.

Yamane, Y., Kaneda, Y. & Doi, M. 1994 Numerical simulation of semi-dilute suspensions of rodlike particles in shear flow. *J. Non-Newtonian Fluid Mech.* **54**, 405–421.